J. Fluid Mech. (2008), *vol.* 607, *pp.* 81–107.
doi:10.1017/S002211200800181X Printed in the United Kingdom

Flow structure behind two staggered circular cylinders. Part 2. Heat and momentum transport

J. C. HU AND Y. ZHOU†

Department of Mechanical Engineering, The Hong Kong Polytechnic University, Hung Hom, Kowloon, Hong Kong, China

(Received 13 March 2007 and in revised form 7 March 2008)

This work aims to study flow structures, heat and momentum transport in the wake of two staggered circular cylinders. In order to characterize heat transport in the flow, both cylinders were slightly heated so that heat generated could be treated as a passive scalar. The velocity and temperature fluctuations were simultaneously measured by traversing a three-wire (one cross-wire plus one cold wire) probe across the wake, along with a fixed cross-wire, which acted to provide a reference signal. Four distinct flow structures, i.e. two single-street modes (S-I and S-II) and two twin-street modes (T-I and T-II), are identified based on the phase-averaged vorticity contours, sectional streamlines, and their entrainment characteristics. Mode S-I is characterized by a vortex street approximately antisymmetric about the centreline. This mode is further divided into S-Ia and S-Ib, which differ greatly in the strength of vortices. The vortex street of Mode S-II is significantly asymmetric about the centreline, the strenth of vortices near the downstream cylinder exceeding by 50 % that on the other side. Mode T-I consists of two alternately arranged vortex streets; the downstream-cylinder-generated street is significantly stronger than that generated by the upstream cylinder. In contrast, Mode T-II displays two streets approximately antisymmetrical about the wake centreline. Free-stream fluid is almost equally entrained from either side into the wake in Modes S-Ia and T-II, but largely entrained from the downstream cylinder side in Modes S-II and T-I. The entrainment motion in Mode S-Ib is very weak owing to the very weak vortex strength. Vortices decay considerably more rapidly in the twin-street modes, under vigorous interactions between the streets, than in the single-street modes. This rapid decay is particularly evident for the inner vortices near the wake centreline in Modes T-II and T-I. Other than flow structures, heat and momentum transport characteristics are examined in detail. Their possible connection to the initial conditions is also discussed.

1. Introduction

Cylindrical structures in arrays are frequently seen in engineering. The simplest configuration of an array of cylinders is two cylinders in tandem, side-by-side or staggered arrangements. Aerodynamic interference between two cylinders may result in flow separation, reattachment, vortex impingement, recirculation and quasi-periodic vortices, involving most generic flow features associated with multiple cylinders. Thus, flow around two cylinders is a good model for understanding the physics of flow around multiple cylindrical structures.

† Author to whom correspondence should be addressed: mmyzhou@polyu.edu.hk

Numerous investigations have been conducted to study two staggered cylinders in crossflow, mostly focusing on the distributions of mean surface pressure coefficient C_p (e.g. Hori 1959), lift and drag coefficients, C_L and C_d, on the cylinders (e.g. Zdravkovich 1977, 1985, 1987; Price & Païdoussis 1984; Mahir & Rockwell 1996) and Strouhal numbers, St (e.g. Kiya *et al.* 1980; Sumner *et al.* 2000, 2005; Alam & Sakamoto 2005). Hu & Zhou (2008, Part 1) have given the major works in their table 1 and provided a compendium of the previous major accomplishments.

Investigations on the near wake of two staggered circular cylinders were based mostly on flow visualization and limited to a narrow range of the cylinder centre-to-centre spacing (P) and the angle (α) between the incident flow and the line through the cylinder centres (e.g. Suzuki *et al.* 1971; Ishigai *et al.* 1972, 1973; Gu & Sun 1999). Sumner *et al.* (2000) investigated the near wake using flow visualization and particle image velocimetry (PIV) over $P/d = 1.0 \sim 5.0$ (d is the cylinder diameter) and $\alpha = 0^\circ \sim 90^\circ$ for $x/d < 6$ (the origin of coordinate x was defined at the mid-point between the cylinders). They identified nine different flow patterns, depending on P and α, of which three were associated with cylinders in close proximity, three in small α and three in large α. Akbari & Price (2005) investigated numerically the flow around two staggered cylinders at $x/d < 6$. They observed five distinct flow patterns, depending on the geometrical arrangement of the two cylinders. However, little has been known about how these flow structures evolve further downstream, in particular, beyond $x/d = 10$. This information is important when predicting unsteady forces on downstream structures.

Because of the nature of turbulence at a high Reynolds number, neither flow visualization nor instantaneous PIV data could provide a definitive picture of different flow structures. For instance, how does a typical flow structure differ from others in the strength of vortices? What are the topological characteristics of individual typical flow structures? This definitive picture may be extracted from conditionally averaged experimental data. Zhou, Zhang & Yiu (2002) investigated the wake of two side-by-side cylinders at $x/d = 10 \sim 40$ for $P/d = 1.5$ and 3.0 ($Re = 5830$) based on phase-averaged hot-wire data. They documented quantitatively the difference in the flow structure, heat and momentum transport characteristics between the regimes of the asymmetrical wake ($P/d = 1.5$) and two coupled vortex streets ($P/d = 3.0$). Zhou & Yiu (2006) used the same technique to study a two-tandem-cylinder wake at $10d$ to $30d$ behind the downstream cylinder for $P/d = 1.3$, 2.5, 4.0 and 6.0 ($Re = 7000$). They uncovered for the first time two distinct flow structures in the reattachment regime, i.e. at $P/d = 2.5$ and 4.0, depending on whether the shear layers from the upstream cylinder reattach on the downstream or upstream side of the downstream cylinder. It is expected that the flow structure behind two staggered cylinders should differ from that behind two side-by-side or inline cylinders.

One objective of this work is to quantify typical flow structures at $x/d = 10$ and 20 behind two staggered cylinders using the phase-averaging technique as used by Zhou *et al.* (2002) and Zhou & Yiu (2006). Heat and momentum transport characteristics in a two-staggered-cylinder wake are of fundamental interest. Another objective is to understand these characteristics associated with each typical flow structure. Note that 'heat' in this paper is not necessarily the energy in transit. 'Heat' not only represents thermal energy but also simulates a passive scalar. The importance and relevance of passive scalar transport to pollutant transfer, turbulent mixing, combustion and many other engineering applications have been elucidated by Warhaft (2000) and Shraiman & Siggia (2000). Experimental details are provided in § 2. The time-averaged

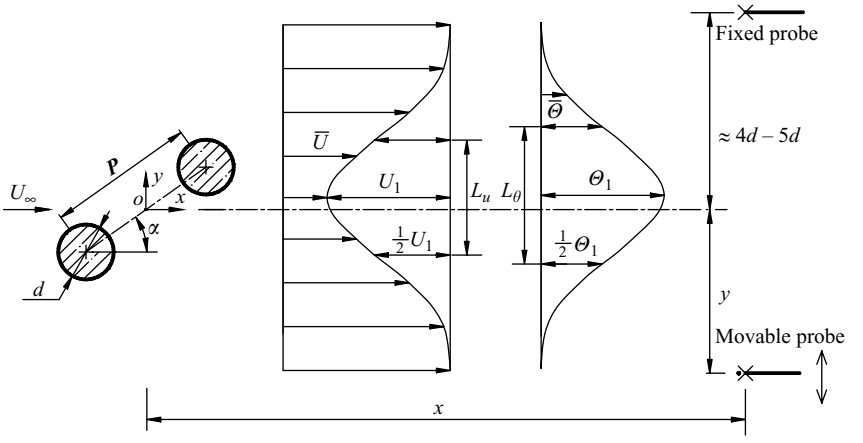

FIGURE 1. Schematic of experimental arrangement.

flow and temperature fields are presented in § 3, followed by the phase-averaged results (§ 4). Section 5 studies the contribution from the coherent structures to the Reynolds stresses and heat fluxes. Heat transport characteristics are discussed in § 6. Finally, conclusions are drawn in § 7.

2. Experimental details

Experiments were performed in a closed-circuit wind tunnel with a 2.4 m long square test section (0.6 m × 0.6 m). See Huang, Zhou & Zhou (2006) for more details of the tunnel. The experimental arrangement is sketched in figure 1. The wake was generated by two brass circular cylinders of the same diameter $d = 12.5$ mm in staggered configurations. Both cylinders were placed horizontally in the mid-plane and spanned the full width of the working section, resulting in a maximum blockage of about 4.2 % and an aspect ratio of 48. The cylinders were arranged at $\alpha = 10^\circ \sim 60^\circ$, with an increment of 10°, for $P/d = 1.2$ and 2.0, respectively, and $\alpha = 10^\circ$ and 50° for $P/d = 4.0$, covering the P/d and α ranges of the nine flow patterns, reported by Sumner *et al.* (2000), in the near wake of two staggered cylinders. Both cylinders were electrically heated. The surface temperature of the cylinders, monitored by thermocouples, was about 36 °C at a free-stream velocity $U_\infty = 8.4\ \mathrm{m\,s^{-1}}$. The room was air-conditioned and maintained at 24 °C during experiments. The maximum mean temperature difference between the heated wake and the ambient fluid did not exceed 1 °C at $x/d \geqslant 10$. The buoyancy effect due to the temperature difference was negligible and heat could be considered as a passive scalar (Matsumura & Antonia 1993). Measurements were carried out at $x/d = 10$ and 20. U_∞ was $8.4\ \mathrm{m\,s^{-1}}$, corresponding to an $Re(\equiv U_\infty d/\nu$, where ν was the kinematic viscosity of the air) of 7000. The wake of an isolated circular cylinder ($P/d = 0$) was also measured in order to provide a benchmark for comparison.

A movable three-wire (one cross-wire plus a cold wire) probe was used to measure simultaneously the velocity and temperature fluctuations across the wake. The cold wire was orientated normal to the plane of the cross-wire and positioned at about 0.8 mm upstream of the cross-wire intersection. This probe measured the fluctuating longitudinal velocity (u), transverse velocity (v) and temperature (θ) at the nominal same point. Another cross-wire was placed on the side near the downstream cylinder at $y/d = 4 \sim 5$, depending on P, α and x, to provide a reference phase signal.

$\overline{U}^*$	$\overline{\Theta}^*$	u^*_{rms}	v^*_{rms}	$\overline{uv}^*$	θ^*_{rms}	St
$\pm 2\%$	$\pm 3\%$	$\pm 6\%$	$\pm 6\%$	$\pm 6\%$	$\pm 5\%$	$\pm 1\%$

TABLE 1. Experimental uncertainties ($x^* = 10$ for y^*_c, U^*_c and $\tilde{\omega}^*$).

The sensors of the cross-wires were made of 5 μm Wollaston wire (Pt-10 % Rh) of approximate 1 mm in length, operated on constant temperature circuits at an overheat ratio of 1.5. The cross-wires were calibrated in terms of effective yaw angles and velocity before and after data sampling. The cold wire, made of Wollaston wire (Pt-10 % Rh), was 1.27 μm in diameter and about 1.2 mm in length, operated on a constant current (0.1 mA) circuit with an output linearly proportional to θ. The temperature coefficient of the cold wire was estimated to be 1.69×10^{-3} °C^{-1}. The velocity and temperature signals were simultaneously acquired, offset, amplified and digitized using a 16 channel (12 bit) A/D board on a personal computer at a sampling frequency, $f_{sampling}$, of 3000 Hz per channel. The sampling duration was 20 s.

Table 1 gives estimated experimental uncertainties in $\overline{U}$, $\overline{\Theta}$, u_{rms}, v_{rms}, and θ_{rms}, where U is the instantaneous streamwise velocity, Θ is the instantaneous temperature, the overbar and subscript *rms* represent time-averaged and root-mean-square values, respectively. The uncertainties of u_{rms} and v_{rms} were inferred from the errors of the hot-wire calibration data, whereas those of $\overline{\Theta}$ and θ_{rms} were largely due to errors caused by the slight drift of the cold wire during measurements and a possible change of the surrounding conditions. In this paper, an asterisk is used to denote normalization by U_∞, d and/or the maximum mean temperature excess, Θ_1, in the wake.

3. Time-averaged flow and temperature fields

In view of the observation of four typical flow structures behind two staggered cylinders for $P^* = 1.2 \sim 4.0$ and $\alpha = 0° \sim 90°$ (Part 1), data will be presented for five configurations, i.e. $P^* = 1.2$ at $\alpha = 30°$, 4.0 at 10°, 2.0 at 40°, 4.0 at 50° and 3.0 at 90°, corresponding to modes S-Ia, S-Ib, S-II, T-I, T-II, respectively. Mode T-II is extracted from Zhou *et al.* (2002).

Figure 2 presents the cross-stream distributions of the mean velocity deficit $1 - \overline{U}^*$ and $\overline{\Theta}^*$ at $x^* = 10$ and 20. The distributions of $1 - \overline{U}^*$ and $\overline{\Theta}^*$ display a single peak for Modes S-Ia, S-Ib and S-II, conforming to the occurrence of one single vortex street. The $\overline{\Theta}^*$ distribution is asymmetric about the wake centreline (figure 2*f*) for Mode S-II, indicating an asymmetric wake. In contrast, $1 - \overline{U}^*$ and $\overline{\Theta}^*$ (figure 2*a–d*) for Mode S-I are roughly symmetric about the centreline, implying a reasonably antisymmetric flow structure. On the other hand, $1 - \overline{U}^*$ and $\overline{\Theta}^*$ (figure 2*g*, *h*) for Mode T-I show a twin-peak distribution, suggesting the occurrence of two vortex streets. The two peaks in $1 - \overline{U}^*$ are different in magnitude, in contrast with the case for Mode T-II (figure 2*i*, *j*), where the two peaks exhibit approximately the same magnitude. Apparently, the wake is asymmetric about $y^* = 0$ for Mode T-I.

The major characteristic parameters of the mean flow and temperature fields are summarized in table 2. In general, both U^*_1 and Θ_1 decrease from $x^* = 10$ to 20. Meanwhile, the mean velocity half-width, L_u, grows by 46 %, 36 %, 13 %, 11 %

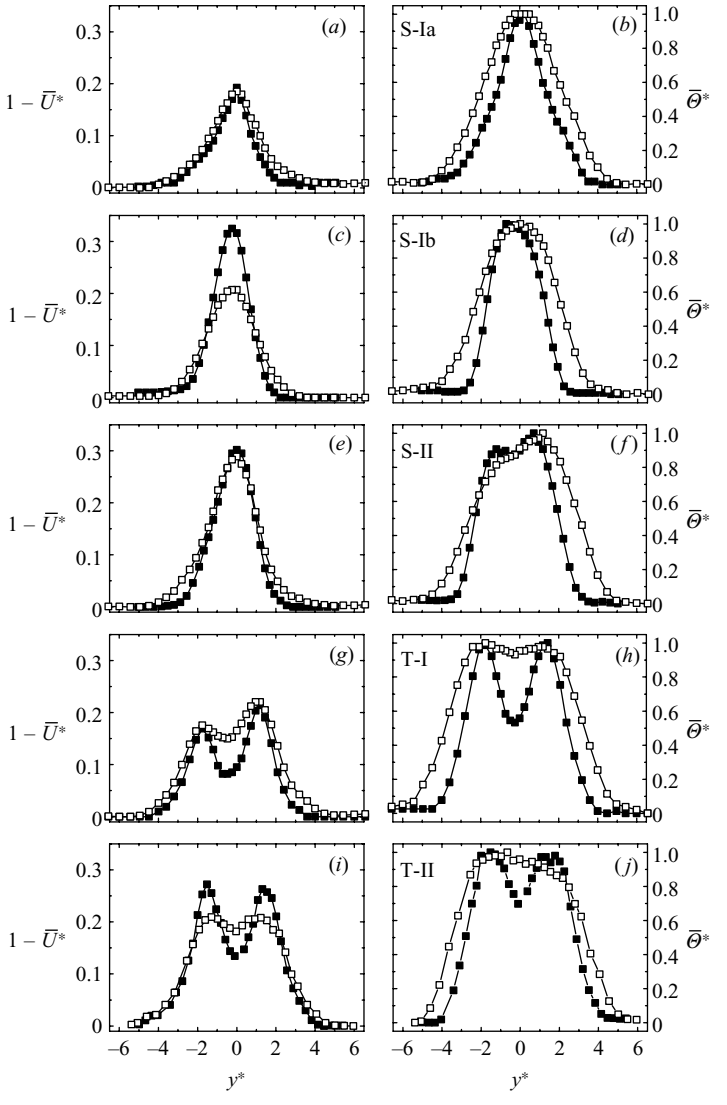

FIGURE 2. Time-averaged streamwise velocity deficit $1-\overline{U}^*$ and temperature $\overline{\Theta}^*$: (*a*, *b*) Mode S-Ia ($P^*=1.2$, $\alpha=30°$); (*c*, *d*) S-Ib (4.0, 10°); (*e*, *f*) S-II (2.0, 40°); (*g*, *h*) T-I (4.0, 50°); (*i*, *j*) T-II (3.0, 90°). ■, $x^*=10$; □, 20.

and 15 % for Modes S-Ia, S-Ib, S-II, T-I and T-II, respectively. The corresponding increase in the mean temperature half-width, L_θ, is 49 %, 38 %, 12 %, 33 % and 22 %, respectively. The difference indicates that the symmetric single vortex street (e.g. Mode S-I) grows faster than the asymmetric (S-II). The wake grows approximately at the same rate (about 12 %) in L_u for Modes S-II and T-I, but less rapidly in L_θ for S-II than for T-I. The observation suggests that interactions between two vortex streets enhance the diffusion of passive scalar (heat). It is worth mentioning that L_θ is larger than L_u, regardless of the values of P, α or x. It may be concluded that the lateral growth in $\overline{\Theta}^*$ is faster than that in $1-\overline{U}^*$ in a two-staggered-cylinder wake.

	S-I									
Mode	S-Ia		S-Ib		S-II		T-I		T-II	
P^*	1.2		4.0		2.0		4.0		3.0	
α(deg.)	30		10		40		50		90	
x^*	10	20	10	20	10	20	10	20	10	20
U_1^*	0.19	0.18	0.32	0.21	0.3	0.29	0.21	0.22	0.28	0.21
Θ_1(°C)	0.78	0.6	0.83	0.72	0.87	0.62	0.77	0.67	0.69	0.48
L_u^*	1.9	2.77	2.12	2.89	2.39	2.71	4.47	4.98	4.79	5.53
L_θ^*	2.81	4.19	3.09	4.25	4.59	5.16	5.4	7.16	5.67	6.89

TABLE 2. Maximum velocity defect, temperature excess and half-width.

4. Phase-averaged flow and temperature fields

4.1. *Phase-averaging technique*

Since Mode T-II is discussed in detail in Zhou *et al.* (2002), the results of this mode, unless otherwise stated, will not be repeated. The power spectral density functions, E_u, E_v and E_θ (not shown), of signals u, v and θ measured at $x^* = 10$ and 20 behind two staggered cylinders display one pronounced peak at $St(\equiv f_s d/U_\infty) = 0.128$, 0.178, 0.143 and 0.192 for Modes S-Ia, S-Ib, S-II and T-I, respectively, indicating the occurrence of large-scale quasi-periodic events.

Careful examination on the v-signal from the three-wire probe at $y^* = 1$ and the simultaneously acquired reference v_R-signal obtained from the fixed cross-wire at $y^* \approx 4$ reveals a phase correlation in large-scale events between v and v_R (not shown). Figure 6 in Zhou & Yiu (2006) gives examples. Thus, the velocity and temperature fluctuations are phase-averaged based on the phase signal, i.e. v_R. This technique has been discussed in detail in Matsumura & Antonia (1993), Zhou *et al.* (2002) and Zhou & Yiu (2006), and thus not repeated here.

Since the vortex shedding frequency is not strictly a constant, it is subjected to variation from one cycle to another, which is particularly significant at high *Re*. This variation is connected to the random oscillation of the point of flow separation from circular cylinders and the nature of turbulence, resulting in a phase jitter and errors in phase-averaging. To minimize this phase jitter and its effect, v_R was collected at the same downstream station as u, v and θ (e.g. Kiya & Matsumura 1985; Hussain & Hayakawa 1987).

The phase-averaged value of an instantaneous quantity Q is calculated by

$$\langle Q \rangle_k = \frac{1}{N} \sum_{i=1}^{N} Q_{k,i},$$

where k represents phase. For convenience, the subscript k will be omitted hereinafter. N is the total number of detections, around 1500, 2400, 1400 and 2600 for Modes S-Ia, S-Ib, S-II and T-I, respectively. Q can be decomposed into a time-averaged component $\overline{Q}$ and a fluctuating component q. The latter may be further separated into a coherent fluctuation $\tilde{q} \equiv \langle q \rangle$ and a remainder q_r:

$$q = \tilde{q} + q_r,$$

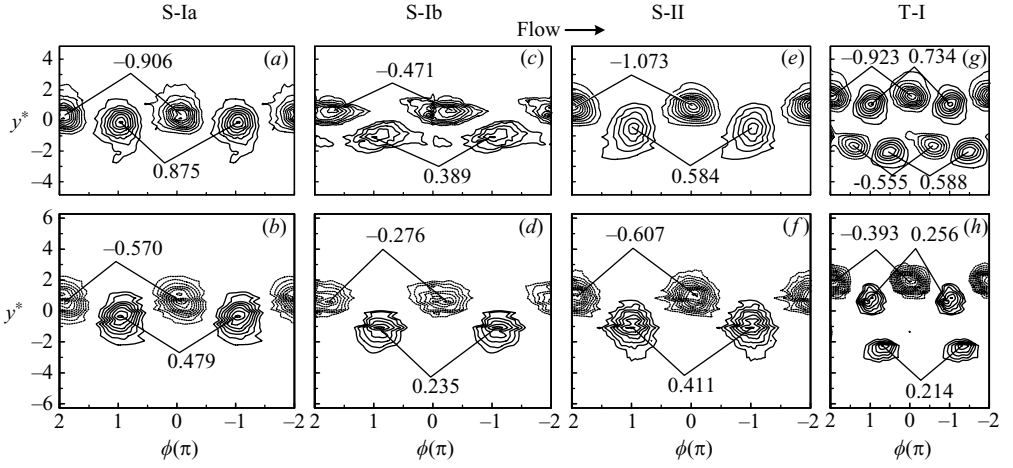

FIGURE 3. Phase-averaged vorticity contours $\tilde{\omega}^*$ (the cutoff level $= \pm 0.1$): (*a*) the contour increment $= 0.1$, (*b*) 0.05, (*c*) 0.05, (*d*) 0.025, (*e*) 0.1, (*f*) 0.05, (*g*) 0.1, (*h*) 0.025. (*a*, *c*, *e*, *g*) $x^* = 10$; (*b*, *d*, *f*, *h*) $x^* = 20$.

and

$$\langle qs \rangle = \tilde{q}\tilde{s} + \langle q_r s_r \rangle,$$

where q and s stand for either u, v or θ.

4.2. *Phase-averaged flow structures*

Figure 3 presents the iso-contours of phase-averaged vorticity for Modes S-Ia, S-Ib, S-II and T-I. Modes S-Ia, S-Ib and S-II are all characterized by one single vortex street, whilst T-I and T-II (not shown) by two streets, conforming to the distributions of $1 - \overline{U}^*$ and $\overline{\Theta}^*$ (figure 2). Note that phase ϕ in figure 3, ranging from -2π to $+2\pi$, may be explicated to be a longitudinal distance, $\phi = 2\pi$ corresponding to the averaged vortex wavelength. To avoid any distortion of the physical space, the same scales are used in the ϕ- and y^*-directions in figure 3 and those that follow.

The flow structure at $P^* = 1.2$ and $\alpha = 30^\circ$ is shown in figure 3(*a*) ($x^* = 10$) and 3(*b*) ($x^* = 20$) to illustrate Mode S-Ia. The two rows of vortices at $x^* = 10$ and 20 exhibit essentially the same strength, which is comparable to that in an isolated cylinder wake. The maximum phase-averaged vorticity strength measured here is 1.12 and 0.48 at $x^* = 10$ and 20 (not shown), respectively, for the isolated cylinder, which is comparable with Zhou *et al.*'s (2002) measurements (1.27 and 0.52, respectively). Flow structures measured at $P^* = 1.2$ and $\alpha = 90^\circ$ by Zhou *et al.* (2002) and at $P^* = 1.3$ and $\alpha = 0^\circ$ by Zhou & Yiu (2006) also fall into this mode, whose maximum phase-averaged vorticity $\tilde{\omega}^*_{max}$ is 1.24 and 1.18, respectively, at $x^* = 10$. The difference in $\tilde{\omega}^*_{max}$ between Mode S-Ia and that in the isolated cylinder wake is within 20 %.

The flow structure at $P^* = 4.0$ and $\alpha = 10^\circ$ is shown in figure 3(*c*, *d*) to illustrate Mode S-Ib. The strength of vortices (figure 3*c*) is no more than 40 % of that in an isolated cylinder wake. The flow structure in a two-tandem-circular-cylinder wake ($\alpha = 0^\circ$) reported by Zhou & Yiu (2006) at $P^* = 2.5$ and 6.0 also falls into Mode S-Ib, whose $\tilde{\omega}^*_{max}$ is less than 30 % of that in an isolated cylinder wake. Compared with Mode S-Ia (figure 3*a*), vortices in Mode S-Ib appear longitudinally stretched at

$x^* = 10$ (figure 3*c*). This stretch is not evident at $x^* = 20$ (figure 3*d*). The observation suggests that the vortex formation in Mode S-Ib may not be completed before $x^* = 10$, which is consistent with postponed flow separation from the downstream cylinder (Part 1).

In contrast with Modes S-Ia and S-Ib, which are reasonably antisymmetric about the centreline, Mode S-II (figure 3*e*,*f*) is apparently asymmetric about the centreline; the strength of vortices near the downstream cylinder ($y^* > 0$) is about 50 % larger at $x^* = 10$ (figure 3*e*) than that near the upstream cylinder ($y^* < 0$). The flow structure examined by Zhou *et al.* (2002) at $P^* = 1.5$ and $\alpha = 90^\circ$ is one case of Mode S-II, which displays similarity to that in figures 3*e* and 3*f* in terms of asymmetry, that is, the vorticity strengths differ by about 50 % between the two vortex rows.

Mode T-I (figure 3*g*,*h*) exhibits two distinct streets. The maximum vorticity of the street behind the downstream cylinder is about 40 % larger than that behind the upstream cylinder. The difference is ascribed to different vortex shedding frequencies. The frequency of vortex shedding from the upstream cylinder is higher, implying a shorter time to accumulate vorticity before separation and hence a lower vortex strength, than that from the downstream cylinder. This difference persists at $x^* = 10$ and 20. The vortex street behind the upstream cylinder is significantly impaired at $x^* = 20$. In fact, the inner vortices vanish because of vigorous interactions between the two streets, which will be discussed further in § 4.5.

Mode T-II occurs at $P^* \geqslant 2.5$ and $\alpha \geqslant 88^\circ$, where two symmetric or anti-phased streets are observed at $x^* = 10$ and 20 (figures 4 and 5 of Zhou *et al.* 2002), and the vortex strengths in both streets are approximately the same, which is distinct from Mode T-I.

The vortices in the near wake of two staggered cylinders and those in a self-preserving wake or jet exhibit different behaviours. The vortices of Modes S-Ia, T-I and T-II are characterized by relatively strong periodicity, as is evident by the pronounced sharp peak in E_u (figures 5, 11 and 13 in Part 1). Those of Modes S-Ib and S-II are less quasi-periodical, E_u displaying a relatively broad peak (figures 7 and 9 in Part 1). In a turbulent far wake, vortices tend to occur intermittently and in groups, and are rather quasi-periodical within each group (Mumford 1983; Bisset, Antonia & Browne 1990). The major peak in the u- or v-spectrum appears even broader (e.g. Bisset *et al.* 1990; Zhou, Antonia & Tsang 1998). The deviation between the three types of vortices is connected to a difference in their generation. The vortices of Modes S-Ia, T-I and T-II originate from vortex shedding from the two cylinders, similarly to that in the near wake of an isolated cylinder. Naturally, the quasi-periodicity of these vortices is dictated by the frequency of vortex shedding, which is linked to the wake width or shear-layer thickness (Roshko 1954). The vortex generation in Modes S-Ib and S-II is more complicated because of the postponed flow separation in S-Ib or vigorous interactions between the narrow and wide streets in Mode S-II. In both cases, the shear-layer instability plays a role in the complete formation of vortices (Wang & Zhou 2005; Zhou & Yiu 2006) and hence in the periodicity of these vortices. In a turbulent far wake, the generation of vortices may be ascribed to the shear-layer instability (Wygnanski, Champagne & Marasli 1986), which is different from that in the near wake of a bluff body (e.g. Zhou & Antonia 1995; Zhou *et al.* 2001). The shear-layer instability probably also accounts for the generation of vortices observed in the far field (160 slot heights from the slot where the jet issued) of a turbulent plane jet by Mumford (1982). In fact, Wygnanski & Petersen (1987) noted that the linear modes of instability in a plane cylinder wake were the same as the plane jet. It may be inferred that the quasi-periodicity of vortices in the far field of a turbulent

wake or jet could be determined by the shear-layer instability frequency, which is probably related to the wake or jet width.

4.3. *Multiple dominant frequencies of large-scale vortical structures*

Mode T-I is characterized by two dominant frequencies across the wake even up to $x^* = 20$. The lower and higher frequencies dominate at $y^* > 0$ and $y^* < 0$, respectively, ascribed to the alternate vortex shedding from the downstream and upstream cylinders, respectively. Naturally, this begs the question of which frequency should be used as the centre frequency for filtering to obtain the reference phase and how this choice would affect the phase-averaged flow. As such, a reference probe was also placed at $y^* = -4 \sim -5$ (near the upstream cylinder) for $P^* = 4.0$ and $\alpha = 50^\circ$ (Mode T-I). Phase-averaging (Matsumura & Antonia 1993; Zhou *et al.* 2002; Zhou & Yiu 2006) was conducted with the centre frequency set at the two different dominant frequencies. The iso-contours of vorticity and corresponding streamlines at $x^* = 10$ were compared (not shown). When the phase is determined from the reference signal obtained at $y^* \approx 4$, the upper-street vortices in both rows exhibit a higher maximum vorticity than their lower-street counterparts. Once the reference phase is changed to that associated with vortex shedding from the upstream cylinder, as extracted from the reference signal obtained at $y^* \approx -4$, the maximum vorticity of vortices changes slightly, less than 10 % for both rows. This variation is anticipated because of the use of different reference signals. Nevertheless, sectional streamlines (not shown) display qualitatively the same flow structure, without appreciable change in the topological details. The upper-street vortices remain stronger than the lower street ones. Similar observations were made at $x^* = 20$ (not shown). In the following, the phase-averaged data are presented based on the reference phase extracted from the reference signal obtained at $y^* \approx 4$.

4.4. *Characteristic properties of vortices*

The phase-averaged vorticity is calculated by,

$$\tilde{\omega} = \frac{\partial\left(\overline{V} + \tilde{v}\right)}{\partial x} - \frac{\partial\left(\overline{U} + \tilde{u}\right)}{\partial y} \approx \frac{\Delta\tilde{v}}{\Delta x} - \frac{\Delta\left(\overline{U} + \tilde{u}\right)}{\Delta y},$$

where $\overline{V}(\approx 0)$ is the lateral time-averaged velocity, $\Delta x = -U_c \Delta t = -U_c / f_{sampling}$. U_c is the averaged convection velocity of vortices, which is identified with the velocity at the location where $\tilde{\omega}_{max}$ occurs. The most likely vortex position y_c^*, U_c^* and $\tilde{\omega}_{max}^*$ are summarized in table 3 for the four modes of flow structures. Experimental uncertainties for y_c^*, U_c^* and $\tilde{\omega}_{max}^*$ are estimated to be 3 %, 3 % and 6 %, respectively. In this table, 'upper' and 'lower' stand for vortices above and below the centreline, respectively. 'Outer' represents the outer vortices of Modes T-I or T-II, which are shed from the side of a cylinder nearer to the free stream; 'inner' denotes the inner vortices shed from the side of a cylinder close to $y^* = 0$ (figure 1). In general, U_c^* increases with x^*, and U_c^* of the upper vortices is larger than that of the lower. For convenience, U_c^* of the outer vortex is used in Taylor's hypothesis to convert time interval into spatial separation, i.e. $\Delta x = -U_c \Delta t$, and calculation of the averaged vortex wavelength, i.e. $U_c T_s = U_c / f_s$. It has been verified that the phase-averaged results do not differ appreciably when U_c^* is slightly changed, similarly to that observed by Zhou *et al.* (2002) and Zhou & Yiu (2006).

The $\tilde{\omega}_{max}^*$ value (table 3) for Mode S-Ia drops by 37 % and 45 % from $x^* = 10$ to 20 for the upper and lower vortices, respectively. The corresponding drops for Mode S-Ib are 41 % and 39 %, respectively. In contrast, this drop for Mode S-II is 43 % for

			S-I									
Mode			S-Ia		S-Ib		S-II		T-I		T-II	
P^*			1.2		4.0		2.0		4.0		3.0	
α(deg.)			30		10		40		50		90	
		x^*	10	20	10	20	10	20	10	20	10	20
y_c^*	Outer	Upper	0.38	0.65	0.62	0.88	0.89	0.99	1.56	1.94	1.88	2.06
		Lower	−0.12	−0.35	−1.08	−1.25	−0.56	−1.07	−2.03	−2.23	−1.87	−1.97
	Inner	Upper							1.06	0.59	1.24	
		Lower							−1.64		−1.28	
U_c^*	Outer	Upper	0.86	0.87	0.81	0.84	0.81	0.82	0.83	0.85	0.83	0.84
		Lower	0.83	0.84	0.78	0.84	0.74	0.79	0.85	0.85	0.83	0.84
	Inner	Upper							0.80	0.80	0.81	
		Lower							0.85		0.81	
$\tilde{\omega}_{max}^*$	Outer	Upper	−0.91	−0.57	−0.47	−0.28	−1.07	−0.61	−0.92	−0.39	−0.77	−0.28
		Lower	0.88	0.48	0.39	0.24	0.58	0.41	0.59	0.21	0.85	0.33
	Inner	Upper							0.73	0.26	0.63	0.07
		Lower							−0.56		−0.72	−0.11

TABLE 3. The vortex path, convection velocity and maximum vorticity.

the upper vortices, but only 29 % for the lower, suggesting that the vorticity decay rate in the asymmetric wake (Mode S-II) is different between the two rows of vortices, and the vortices of the larger strength decay more rapidly than those of the smaller.

The vortices in Modes T-I and T-II decay faster than in the single-street modes, $\tilde{\omega}_{max}^*$ falling by about 60 % from $x^* = 10$ to 20 for the outer vortices. The inner vortices decay even more rapidly, $\tilde{\omega}_{max}^*$ in Mode T-I dropping by 65 % for the upper inner vortices and by 100 % for the lower. The corresponding drops exceed 80 % for Mode T-II (Zhou *et al.* 2002). The rapid decay leads to the disappearance or substantial impairment of the inner vortices at $x^* = 20$. The observation is ascribed to vigorous interactions between the two vortex streets (Kolář, Lyn & Rodi 1997; Zhou *et al.* 2002).

4.5. *Vorticity transport*

Effective turbulent vorticity flux density vector, $\tilde{J} = \{J^x, J^y\}$, is examined to understand the streamwise evolution of vortices. J^x and J^y are given by Kolář *et al.* (1997):

$$J^x = \frac{\partial}{\partial y}\left[\frac{\langle v_r^2\rangle - \langle u_r^2\rangle}{2}\right] + \frac{\partial}{\partial x}\langle u_r v_r\rangle, \tag{1}$$

$$J^y = \frac{\partial}{\partial x}\left[\frac{\langle v_r^2\rangle - \langle u_r^2\rangle}{2}\right] - \frac{\partial}{\partial y}\langle u_r v_r\rangle. \tag{2}$$

The vector $\tilde{J}^*$ provides a measure for the transport of vorticity (Kolář *et al.* 1997). Figure 4 presents the vectors at $x^* = 10$ and 20. The length of $\tilde{J}^*$ is proportional to the strength of the vorticity flux density. A reference vector and the corresponding magnitude of vorticity flux density are given at the left-hand upper corner in figure 4. To facilitate data interpretation, the outermost $\tilde{\omega}^*$ contours in figure 3 are included

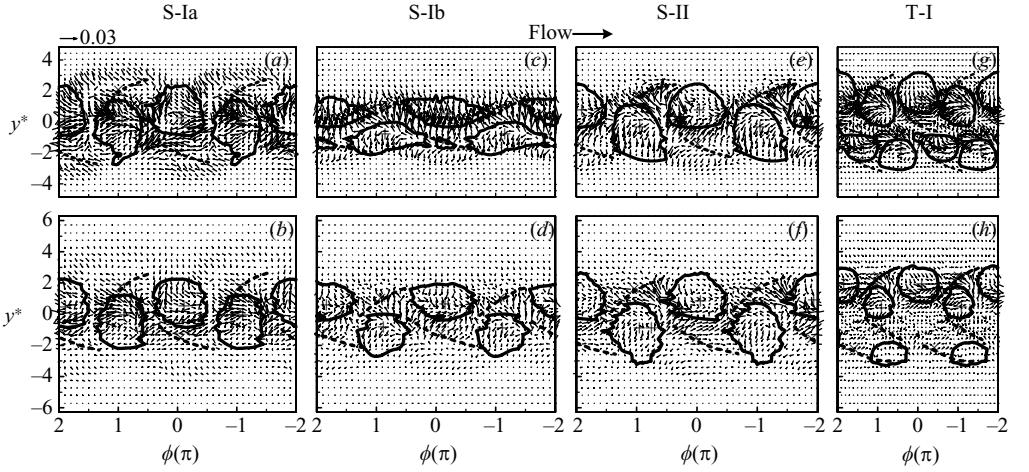

FIGURE 4. Effective vorticity flux density vectors $\tilde{J}^*$. +, centres; ×, saddles. The thicker solid line denotes the outermost vorticity contours in figure 3; the thicker broken line indicates the diverging separatrix. (a, c, e, g) $x^* = 10$; (b, d, f, h) $x^* = 20$.

in the figure (and also those that follow) to indicate the vortex border. Foci and saddle points (e.g. Zhou & Antonia 1994) associated with vortices, determined from sectional streamlines (not shown), are marked by '+' and '×', respectively. The diverging separatrix (Hussain & Hayakawa 1987) through the saddle point is shown by a thick broken line. In general, foci correspond well to the maximum vorticity, in particular, at $x^* = 10$.

In Mode S-Ia, with the two staggered cylinders rather close to each other, the vectors behave similarly to those in a single-cylinder wake (Zhou *et al.* 2002), and relatively long vectors are seen crossing the vortex border, pointing to or reaching the neighbouring vortices (figure 4*a*), in particular, on the downstream side of a vortex (e.g. the one at $\phi = 0$). The observation indicates vigorous vorticity exchange between counter-rotating vortices, accounting for the 40 % drop in $\tilde{\omega}^*_{max}$ from $x^* = 10$ to 20. This drop is lower than that (58 %) in the isolated cylinder case (e.g. Zhou *et al.* 2002). Note that the present St is 0.128, about 40 % lower than in a single cylinder wake, corresponding to a longer vortex wavelength in view of the same U_c^* (0.86), and subsequently implying relatively weak interactions between neighbouring vortices and a reduced decay rate in the vortex strength. Vortices in Mode S-Ib are longitudinally elongated. As a consequence, the cross-stream vortices of opposite sign, though weak in strength, are close to each other along a significant portion of their periphery, enhancing vorticity exchange between the counter-rotating vortices. The vector lengths near the border between adjacent vortices in Mode S-Ib (figure 4*c*) are comparable to those in Mode S-Ia, which is internally consistent with their comparable vorticity decay rates ($\sim$ 40 %) from $x^* = 10$ to 20. In Mode S-II, long vectors mainly cross the border of the upper row vortices generated by the downstream cylinder, e.g. at $\phi = 0$, apparently due to the greater strength of the vortices. Consequently, the upper row vortices decay faster. Relatively long vectors in Mode T-I are mainly associated with the inner vortices for both streets. Some of the vectors in the inner vortices interacts with the vortices of opposite sign in the same street, and some with the inner vortices in the other street. The vorticity exchange characteristics are similar to those in Mode T-II (cf. figure 7 in Zhou *et al.* 2002). Other than interacting with vortices

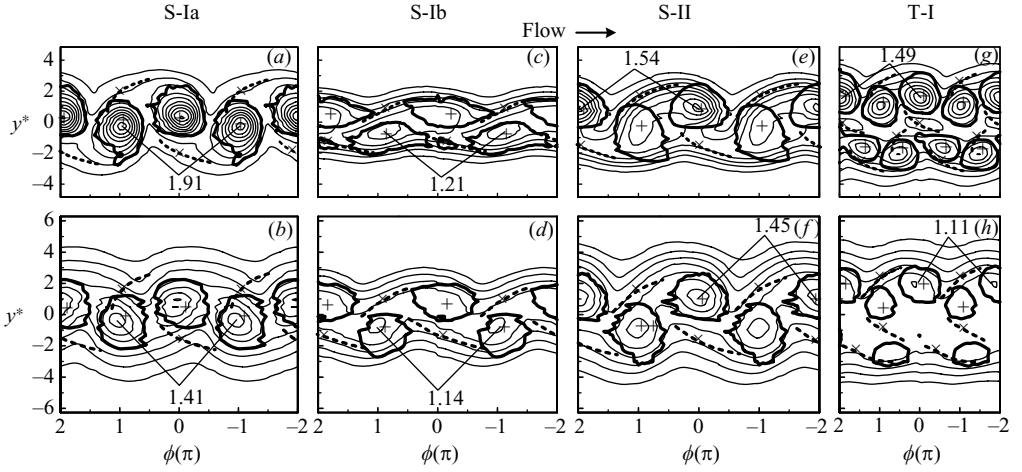

FIGURE 5. Phase-averaged temperature contours $\overline{\Theta}^* + \tilde{\theta}^*$ (the cutoff level = 0.1, the contour interval = 0.2). The thicker solid line denotes the outermost vorticity contours in figure 3; the broken line indicates the diverging separatrix. (a, c, e, g) $x^* = 10$; (b, d, f, h) $x^* = 20$.

shed from the same cylinder, the inner vortices also interact with the inner vortices shed from the other cylinder. On the other hand, the outer vortices interact only with inner vortices in the same street. As a result, the inner vortices decay faster; those in the lower street generated by the upstream cylinder vanish by $x^* = 20$ (figure 3*h*). The inner vortices in the upper street associated with the downstream cylinder persist at $x^* = 20$, probably owing to their initial greater strength. The vorticity exchange characteristics of Mode T-II have been discussed in detail by Zhou *et al.* (2002), and thus are not repeated here. However, it is worth mentioning that the inner vortices in both streets of Mode T-II are equally weakened from $x^* = 10$ to 20, not vanishing until $x^* = 40$.

4.6. *Phase-averaged temperature field*

Figure 5 presents the contours of phase-averaged temperature, $\overline{\Theta^*} + \tilde{\theta}^*$. At $x^* = 10$, the isotherms of $\overline{\Theta^*} + \tilde{\theta}^*$ in general show a close similarity to the $\tilde{\omega}^*$ contours, the higher isotherms coinciding with the large concentrations of $\tilde{\omega}^*$. This observation is ascribed to the tendency of strong vortical motion to retain heat (Matsumura & Antonia 1993). The lower isotherm is drawn in toward the centreline from both sides of the wake, indicating the arrival of cold fluid in the wake from the free stream. Because Modes S-II (figure 5*e*) and T-I (figure 5*g*) are asymmetric about the centreline, more cold fluid is drawn into the wake from the side near the downstream cylinder where vortices are stronger. For Mode S-Ib (figure 5*c*), however, the dissociation of the vortical structure with cold fluid is evident even at $x^* = 10$ probably because of weak vortices in this mode (figure 3*c*). At $x^* = 20$, similarity between the $\overline{\Theta^*} + \tilde{\theta}^*$ and $\tilde{\omega}^*$ contours fades, in particular, for Modes T-I (figure 5*h*) and T-II (figure 8 in Zhou *et al.* 2002), conforming to the weakened vortices.

4.7. *Momentum and heat transport*

4.7.1. *Coherent fluctuating velocities and temperature*

The phase-averaged velocity and temperature fluctuations $\tilde{u}^*$, $\tilde{v}^*$ and $\tilde{\theta}^*$ contours of Mode S-Ia (figure 6*a–c*) resemble those previously reported in the wake of an isolated cylinder (Matsumura & Antonia 1993; Zhou *et al.* 2002). The peak values

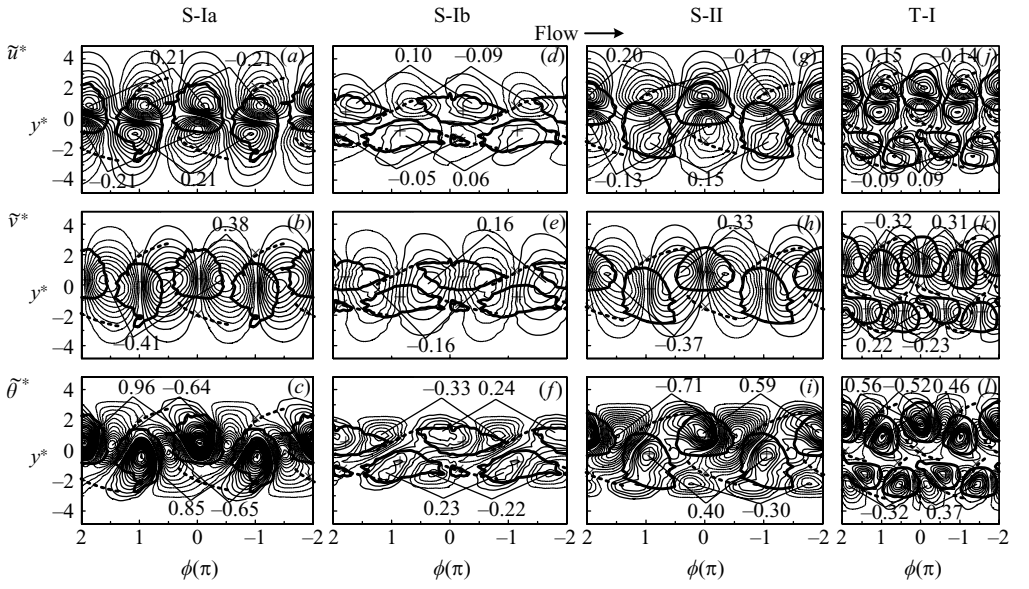

FIGURE 6. Phase-averaged velocity and temperature fluctuations at $x^* = 10$. The contour cutoff level and increment are ± 0.02 and 0.02 for $\tilde{u}^*$, ± 0.04 and 0.04 for $\tilde{v}^*$ and ± 0.05 and 0.05 for $\tilde{\theta}^*$, respectively. The thicker solid line denotes the outermost vorticity contours in figure 3; the broken line indicates the diverging separatrix.

of $\tilde{u}^*$, $\tilde{v}^*$ and $\tilde{\theta}^*$ are the largest of all modes, internally consistent with the strong vorticity strength of Mode S-Ia (figure 3*a*).

Mode S-Ib displays disparities in the $\tilde{u}^*$, $\tilde{v}^*$ and $\tilde{\theta}^*$ contours (figure 6*d–f*) from Mode S-Ia. The $\tilde{u}^*$ contours fail to display up–down anti-symmetry about the vortex centre at $x^* = 10$, which is consistent with the relatively low strength of vortices (figure 3*c*). This up–down anti-symmetry of the $\tilde{u}^*$ contours is, however, seen at $x^* = 20$ (not shown). The observation again suggests that the vortex formation may not be completed at $x^* = 10$. The incomplete vortex formation is probably responsible for not so smooth $\tilde{v}^*$ contours (figure 6*e*), whose maximum level is less than half of that associated with Mode S-Ia. The maximum $\tilde{\theta}^*$ (figure 6*f*) does not coincide with the maximum $\tilde{\omega}^*$, with only part of the positive $\tilde{\theta}^*$ contours overlapping with the vortex, suggesting that warm fluid and vortex are not so closely associated with each other as Mode S-Ia. Furthermore, the longer axis of the higher isotherms tends to be aligned with that of the $\tilde{\omega}^*$ contours, which is inclined with respect to the free stream. In contrast, the longer axis of the higher isotherms or $\tilde{\omega}^*$ contours of Mode S-Ia is approximately normal to the flow direction. At $x^* = 20$, the longer axis of the higher isotherms of Mode S-Ib (not shown) approaches, compared with that at $x^* = 10$, the direction normal to the free stream, pointing again to the fact that the vortex formation may not be completed at $x^* = 10$.

The $\tilde{u}^*$, $\tilde{v}^*$ and $\tilde{\theta}^*$ contours (figure 6*g–i*) of Mode S-II resemble qualitatively their counterparts of Mode S-Ia. Nevertheless, the maximum $\tilde{u}^*$ associated with the lower-row vortices is smaller than its counterpart of Mode S-Ia, apparently because the lower-row vortices are weaker than the upper in Mode S-II, which have comparable strength to that of vortices in Mode S-Ia. By the same token, the maximum $\tilde{v}^*$ and $\tilde{\theta}^*$ of Mode S-II are smaller than their counterparts of Mode S-Ia. The upper-row vortex, e.g. the one at $\phi = 0$, is flanked downstream with the negative $\tilde{\theta}^*$ contours,

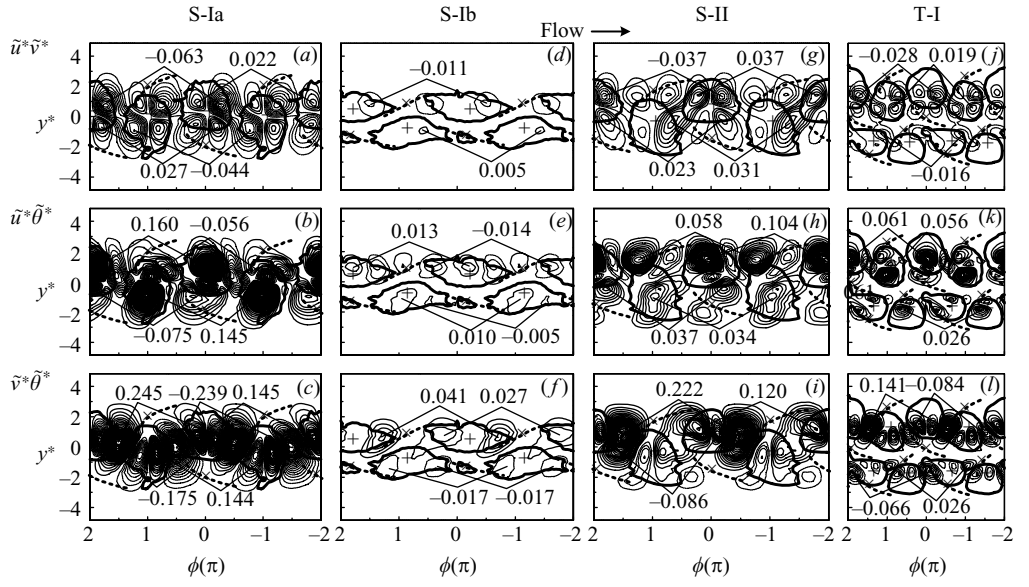

FIGURE 7. Phased-averaged coherent shear stress and heat fluxes ($x^* = 10$). The contour cutoff level and increment are ± 0.005 and 0.005 for $\tilde{u}^*\tilde{v}^*$, ± 0.005 and 0.005 for $\tilde{u}^*\tilde{\theta}^*$, and ± 0.01 and 0.01 for $\tilde{v}^*\tilde{\theta}^*$, respectively. The thicker solid line denotes the outermost vorticity contours in figure 3; the broken line indicates the diverging separatrix.

which penetrate and completely separate the positive $\tilde{\theta}^*$ contours associated with the two opposite-signed cross-stream vortices (figure 6*i*). The lower-row vortex, e.g. at $\phi = -1$, however, is not flanked with the negative $\tilde{\theta}^*$ contours. The difference suggests that the downstream-cylinder-generated vortex is largely responsible for entraining cold fluid into the wake.

In Mode T-I, the $\tilde{u}^*$, $\tilde{v}^*$ and $\tilde{\theta}^*$ contours (figure 6*j–l*) in each street appear qualitatively similar to those in Mode S-Ia, though with considerably smaller maximum levels. The maximum $\tilde{u}^*$, $\tilde{v}^*$ and $\tilde{\theta}^*$ associated with the downstream-cylinder-generated vortex street ($y^* > 0$) are larger than those associated with the other street ($y^* < 0$) because of the difference in their vortex strengths. In contrast, these maxima of the two streets are essentially the same for Mode T-II (see figure 9 in Zhou *et al.* 2002).

4.7.2. *Coherent momentum and heat fluxes*

For Mode S-Ia, the contours of $\tilde{u}^*\tilde{v}^*$, $\tilde{u}^*\tilde{\theta}^*$ and $\tilde{v}^*\tilde{\theta}^*$ (figure 7*a–c*) resemble qualitatively those in an isolated cylinder wake reported by Matsumura & Antonia (1993). In the isolated cylinder case, $\tilde{u}^*\tilde{v}^*$ is almost antisymmetric longitudinally about $\phi = 0$, resulting in a small contribution to $\overline{uv}$ since the positive and negative $\tilde{u}^*\tilde{v}^*$ tend to cancel each other. This antisymmetry is still evident in Mode S-Ia. However, there is an appreciable difference in magnitude between the positive and negative $\tilde{u}^*\tilde{v}^*$, implying an increased contribution to $\overline{uv}$, as confirmed in § 5. The $\tilde{u}^*\tilde{\theta}^*$ contours are dominated by positive contours within the vortex, reflecting the close association of positive $\tilde{u}$ with warm fluid ($\tilde{\theta} > 0$). The $\tilde{v}^*\tilde{\theta}^*$ contours within the vortex are approximately antisymmetric longitudinally about the vortex centre, which is ascribed to the association of both positive and negative $\tilde{v}$ (figure 6*b*) with warm fluid.

The clover-leaf pattern is not evident in the $\tilde{u}^*\tilde{v}^*$ contours of Mode S-Ib (figure 7*d*) as a result of weak vortical structures (figure 3*c*). The negative and positive $\tilde{u}^*\tilde{v}^*$ are predominant at $y^* > 0$ and $y^* < 0$, respectively. This may not necessarily mean a significant contribution to $\overline{uv}$ because of the small magnitude of $\tilde{u}^*\tilde{v}^*$, as compared with Mode S-Ia, which will be confirmed in § 5. In contrast with Mode S-Ia, the positive $\tilde{u}^*\tilde{\theta}^*$ (figure 7*e*) is less dominant within the vortex because weak vortical motion could not retain heat well. The positive $\tilde{v}^*\tilde{\theta}^*$ contours (figure 7*f*) dominate at $y^* > 0$ because of the difficulty for negative $\tilde{v}^*\tilde{\theta}^*$ to survive given $\partial\Theta/\partial y < 0$. By the same token, the negative $\tilde{v}^*\tilde{\theta}^*$ overwhelms the positive at $y^* < 0$, where $\partial\Theta/\partial y > 0$.

The $\tilde{u}^*\tilde{\theta}^*$ and $\tilde{v}^*\tilde{\theta}^*$ contours of Mode S-II (figure 7*g–i*) exhibit more similarity to their counterparts of Mode S-Ia than to those of Mode S-Ib. Nevertheless, the flow structure is significantly asymmetric about the centreline (figure 3*e*). This asymmetry is reflected in the contours, in particular, of $\tilde{u}^*\tilde{\theta}^*$ and $\tilde{v}^*\tilde{\theta}^*$. The $\tilde{u}^*\tilde{v}^*$ contours are rather anti-symmetric longitudinally about the vortex centre for $y^* > 0$, but not so for $y^* < 0$, implying a pronounced contribution to $\overline{uv}$ below the centreline, as confirmed in § 5. The positive $\tilde{v}^*\tilde{\theta}^*$ (figure 7*i*) overwhelms the negative since upper vortices are strongly coherent, accounting for most of the entrainment of cold fluid from the free stream into the wake (figure 5*e*).

The $\tilde{u}^*\tilde{v}^*$, $\tilde{u}^*\tilde{\theta}^*$ and $\tilde{v}^*\tilde{\theta}^*$ contours (figure 7*j–l*) of mode T-I in the upper street behave similarly, albeit to a lesser extent in the lower street, to their counterparts of Mode S-Ia. The $\tilde{u}^*\tilde{v}^*$ contours of the upper street are characterized by a clover-leaf pattern, with negative $\tilde{u}^*\tilde{v}^*$ predominant. The maximum magnitude of $\tilde{u}^*\tilde{v}^*$ is smaller in the lower street, and the positive $\tilde{u}^*\tilde{v}^*$ contours are barely noticeable. The $\tilde{u}^*\tilde{\theta}^*$ and $\tilde{v}^*\tilde{\theta}^*$ contours (figure 7*k*,*l*) display considerable difference between the streets. In particular, the outer vortices (e.g. at $\phi = 0$ of figure 7*l*) of the upper street is flanked downstream, as Mode S-Ia, with a concentration of positive $\tilde{v}^*\tilde{\theta}^*$, indicating a strong entrainment of cold fluid from the free stream. However, there is only a weak concentration of negative $\tilde{v}^*\tilde{\theta}^*$ downstream of the outer vortices (e.g. at $\phi = 0.5$ of figure 7*l*) in the lower street, suggesting a weak entrainment of cold fluid from the free stream. The disparity apparently arises from distinct vortex strengths between the streets (figure 3*g*). In contrast, the $\tilde{u}^*\tilde{v}^*$, $\tilde{u}^*\tilde{\theta}^*$ and $\tilde{v}^*\tilde{\theta}^*$contours (figure 10*g–i* in Zhou *et al.* 2002) of Mode T-II are antisymmetrical about the flow centreline because of the antisymmetry of the two vortex streets.

4.7.3. *Incoherent momentum and heat flux*

The contours of incoherent momentum and heat fluxes, $\langle u_r^* v_r^* \rangle$, $\langle u_r^* \theta_r^* \rangle$ and $\langle v_r^* \theta_r^* \rangle$ (figure 8*a–c*), for Mode S-Ia qualitatively resemble those in an isolated cylinder wake (cf. figure 7*a*, *d*, *g* of Matsumura & Antonia 1993). The maximum concentration of $\langle u_r^* v_r^* \rangle$ tends to occur near the vortex centre, as observed by Zhou *et al.* (2002) and Zhou & Yiu (2006). There is a significant portion of $\langle u_r^* v_r^* \rangle$ distributed along the diverging separatrix through the saddle point, resulting from vortex stretching. The positive and negative concentrations of $\langle u_r^* \theta_r^* \rangle$ (figure 8*b*) or $\langle v_r^* \theta_r^* \rangle$ (figure 8*c*) occur side-by-side and mostly within vortices, with a very weak presence along the diverging separatrix. Above the centreline, $v_r^* \theta_r^*$ tends to be positive because of the association of relatively cold fluid ($\theta_r^* < 0$) with the downward motion ($v_r^* < 0$) or relatively warm fluid ($\theta_r^* > 0$) with the upward motion ($v_r^* > 0$), as inferred from the distribution of $\overline{\Theta}$ (figure 2*b*). Based on experimental data in a single-cylinder wake, Cantwell & Coles (1983) and Hussain & Hayakawa (1987) suggested that potential fluid drawn from the free stream by a vortex may be partially assimilated into the vortex on the other side of the wake. This may have contributed to the presence of the negative

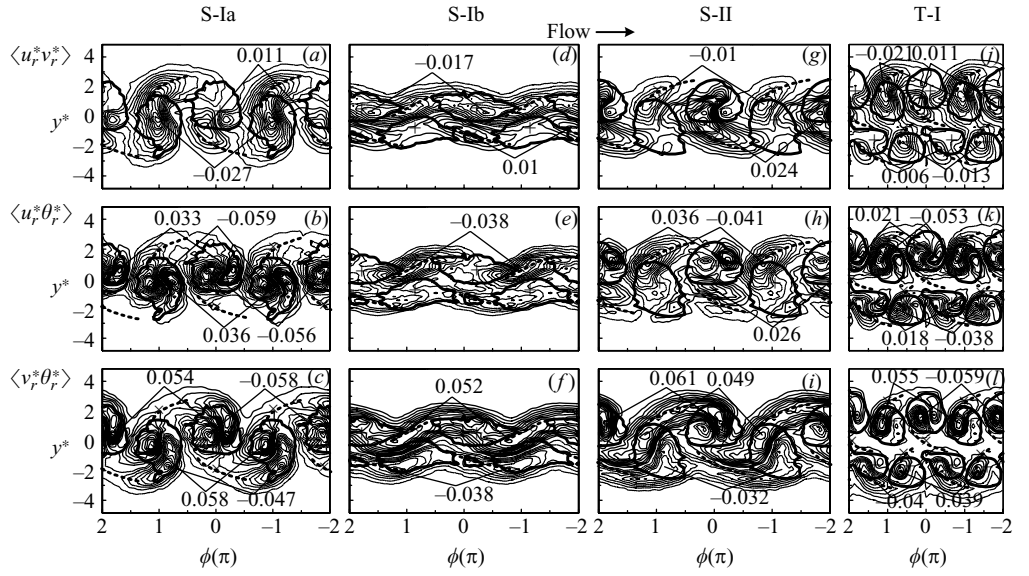

FIGURE 8. Phased-averaged incoherent shear stress and heat fluxes ($x^* = 10$). The contour cutoff level and increment are ± 0.002 and 0.002 for $< u_r^* v_r^* >$, ± 0.004 and 0.004 for $\langle u_r^* \theta_r^* \rangle$, and ± 0.005 and 0.005 for $\langle v_r^* \theta_r^* \rangle$, respectively. The thicker solid line denotes the outermost vorticity contours in figure 3; the broken line indicates the diverging separatrix.

concentrations of $\langle v_r^* \theta_r^* \rangle$ (positive v_r associated with negative θ_r), e.g. upstream of the vortex at $\phi = 0$. On the other hand, $v_r^* \theta_r^*$ tends to be negative below the centreline, but potential fluid drawn from the free stream by the vortex above the centreline is partially assimilated into the vortex below the centreline, resulting in the positive concentrations of $\langle v_r^* \theta_r^* \rangle$ (negative v_r associated with negative θ_r). The observation suggests that incoherent heat fluxes are probably mostly connected to intermediate- to small-scale turbulent structures (Rinoshika & Zhou 2005) that occur within the large-scale vortical structures, with little contribution from the saddle region.

Unlike Mode S-Ia, there is no close association between the $\langle u_r^* v_r^* \rangle$ concentrations (figure 8*d*) and vortices in Mode S-Ib, apparently owing to the very low strength of the vortices (figure 3*c*). Similarly to Mode S-Ia, there is concentrated $\langle u_r^* v_r^* \rangle$ aligned with the diverging separatrix, suggesting that the saddle region is largely responsible for the production of $\langle u_r^* v_r^* \rangle$ in Mode S-Ib. Negative $\langle u_r^* \theta_r^* \rangle$ is predominant (figure 8*e*). While the positive $\langle v_r^* \theta_r^* \rangle$ (figure 8*f*) overwhelms the negative for the upper row of vortices, the opposite is observed for the lower row of vortices. The maximum magnitudes of $\langle u_r^* v_r^* \rangle$, $\langle u_r^* \theta_r^* \rangle$ and $\langle v_r^* \theta_r^* \rangle$ exceed appreciably their coherent counterparts (figure 7*d–f*), whereas Mode S-Ia is the other way around. The observation is reasonable since weak vortices are not expected to play a predominant role in momentum and heat transport.

The $\langle u_r^* v_r^* \rangle$, $\langle u_r^* \theta_r^* \rangle$ and $\langle v_r^* \theta_r^* \rangle$ contours (figure 8*g–i*) of Mode S-II are distinct from those of Mode S-Ia or S-Ib. While concentrated along the separatrix, $\langle u_r^* v_r^* \rangle$ (figure 8*g*) shows concentration within the stronger upper vortex, e.g. the one at $\phi = 0$. Above the centreline, the positive and negative $\langle u_r^* v_r^* \rangle$ contours occur over comparable longitudinal extent and may act to partially cancel each other. Below the centreline, however, the positive $\langle u_r^* v_r^* \rangle$ is predominant, implying a significant contribution from the incoherent motion to $\overline{uv}$, as confirmed in § 5. The $\langle u_r^* \theta_r^* \rangle$ contours above the

centreline are rather different from those below because of the asymmetry of the wake. The $\langle v_r^* \theta_r^* \rangle$ contours (figure 8*i*) within the vortex appear similar to those of mode S-Ia. Nevertheless, $\langle v_r^* \theta_r^* \rangle$ is more concentrated along the separatrix, similarly to Mode S-Ib.

In Mode T-I, the maximum magnitudes of $\langle u_r^* v_r^* \rangle$, $\langle u_r^* \theta_r^* \rangle$ and $\langle v_r^* \theta_r^* \rangle$ are smaller than their coherent counterparts. Because of the asymmetry of the flow structure about $y^* = 0$ (figure 3*g*), $\langle u_r^* v_r^* \rangle$ is considerably more concentrated at $y^* > 0$ than at $y^* < 0$, in contrast with the antisymmetric distribution of positive and negative $\langle u_r^* v_r^* \rangle$ contours about the wake centreline in mode T-II (see figure 11 in Zhou *et al.* 2002).

5. Reynolds stresses, heat fluxes and coherent contributions

5.1. *Structural averaging*

The coherent and incoherent contributions to the Reynolds stresses, temperature variance and heat fluxes may be estimated in terms of structural averaging. Assuming that the phase-averaged structure begins at sample m_1 (corresponding to $\phi = -\pi$) before $\phi = 0$ and ends at sample m_2 (corresponding to $\phi = \pi$) after $\phi = 0$, the structural averaging denoted by a double overbar is defined by

$$\overline{\overline{\tilde{q}\tilde{s}}} = \frac{1}{m_1 + m_2 + 1} \sum_{-m_1}^{m_2} \tilde{q}\tilde{s}.$$

The value of $m_1 (= m_2)$ is 30 so that the duration $(m_1 + m_2 + 1)$ corresponds approximately to one vortex shedding period. The ratio of $\overline{\overline{\tilde{q}\tilde{s}}}$ to $\overline{qs}$ provides a measure to quantify contributions from large-scale coherent structures to momentum and heat transport.

5.2. *Fluctuating velocity and temperature variances*

Figure 9(*a–l*) displays the cross-stream distributions of fluctuating velocity and temperature variances measured at $x^* = 10$, along with their coherent and incoherent contributions. A few observations can be made. (i) $\overline{u^{*2}}$ (figure 9*a–d*), $\overline{v^{*2}}$ (figure 9*e–h*) and $\overline{\theta^{*2}}$ (figur 9*i–l*) are roughly symmetric about $y^* = 0$ for Mode S-Ia. However, the quantities are in general appreciably larger at $y^* > 0$ than $y^* < 0$ for Modes S-Ib, S-II and T-I. The observation is connected with the vortices shed from the downstream cylinder (located at $y^* > 0$) having a strength considerably larger than those shed from the upstream cylinder located at $y^* < 0$ (not shown here). (ii) $\overline{u^{*2}}$ displays two distinct peaks for Modes S-Ia and S-II (figur 9*a*, *c*) but merely one peak for Mode S-Ib (figrue 9*b*). This is because the vortex formation is probably incomplete and vortices are very weak at $x^* = 10$ for Mode S-Ib. This assertion is supported by very weak coherent contributions in this mode, i.e. $\overline{\overline{\tilde{u}^2}}/\overline{u^2}$ (figure 9*b*), $\overline{\overline{\tilde{v}^2}}/\overline{v^2}$ (figure 9*f*) and $\overline{\overline{\tilde{\theta}^2}}/\overline{\theta^2}$(figure 9*j*), as compared with others; the incoherent contribution accounts most for $\overline{u^{*2}}$, $\overline{v^{*2}}$ and $\overline{\theta^{*2}}$. (iii) in contrast with the single street cases, $\overline{\overline{\tilde{u}^{*2}}}$ of Mode T-I exhibits four peaks for $\overline{\overline{\tilde{u}^{*2}}}$ (figure 9*d*) and two peaks for $\overline{\overline{\tilde{v}^{*2}}}$ or $\overline{\overline{\tilde{\theta}^{*2}}}$ (figure 9*h*, *l*), similarly to mode T-II (cf. figure 12, Zhou *et al.* 2002), which is coincident with the occurrence of two vortex streets. (iv) $\overline{\overline{\tilde{v}^2}}/\overline{v^2}$ inferred from figure 9 is largest, compared with $\overline{\overline{\tilde{u}^2}}/\overline{u^2}$ or $\overline{\overline{\tilde{\theta}^2}}/\overline{\theta^2}$, as observed from a single-cylinder wake (Kiya & Matsumura 1985; Matsumura & Antonia 1993). This is not unexpected because $\tilde{v}$ overwhelms $\tilde{u}$ in the near wake owing primarily to the alternate arrangement of counter-rotating

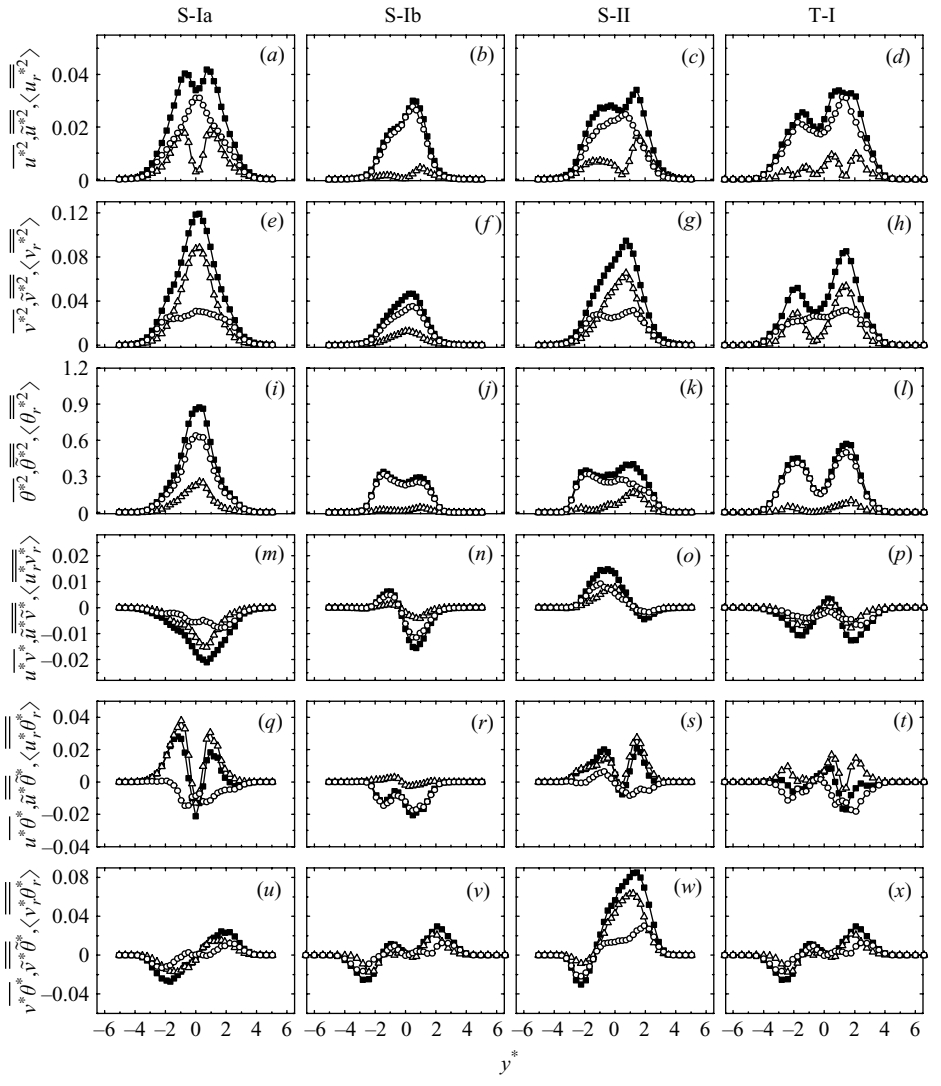

FIGURE 9. ■, Time-averaged, △, coherent and ○, incoherent fluctuating velocity, temperature variances, shear stresses and heat fluxes at $x^* = 10$.

vortices. Furthermore, the present phase-averaging technique identifies vortices based on the v-signal, thus underestimating the coherent contributions to $\overline{u^2}$ and $\overline{\theta^2}$. (v) $\overline{\overline{\tilde{\theta}^{*2}}}$ (figure 9*l*) of mode T-I is much smaller at $|y^*| < 1.5$ than at $|y^*| > 1.5$, similarly to Zhou *et al.*'s (2002) observation for Mode T-II (cf. their figure 14*o*), suggesting a faster loss of heat from inner vortices than from outer ones, internally consistent with the fast vorticity decay rate of inner vortices (§ 4).

5.3. *Reynolds shear stress and heat fluxes*

The cross-flow distribution of $\overline{u^* v^*}$ is approximately symmetric and anti-symmetric about the centreline for Modes S-Ia (figure 9*m*) and T-II (figure 12 of Zhou *et al.* 2002), respectively. This symmetry or anti-symmetry is absent for Modes S-Ib, S-II and T-I (figure 9*n–p*). Note that $\overline{uv}$, $\overline{\overline{\tilde{u}^* \tilde{v}^*}}$ and $\overline{\overline{\langle u_r^* v_r^* \rangle}}$ are negative at $y^* < 0$ in Mode

S-Ia (figure 9*m*), in contrast to their counterparts in an isolated cylinder wake (cf. figure 12*d* in Zhou *et al.* 2002), which are positive below the centreline. Evidently, although the two cylinders in Mode S-Ia behave like a single body, generating a vortex street similar to that behind an isolated cylinder, the momentum transports between the flows are quite different. For Mode S-Ib, the $\tilde{u}^*\tilde{v}^*$ magnitude (figure 7*d*) is small, compared with that of $\langle u_r^* v_r^* \rangle$ (figure 8*d*). Furthermore, the $\langle u_r^* v_r^* \rangle$ contours are predominantly negative at $y^* > 0$ and positive at $y^* < 0$. As a result, $\overline{\overline{\langle u_r^* v_r^* \rangle}}$ accounts for most of $\overline{u^* v^*}$ (figure 9*n*), which is negative at $y^* > 0$ and positive at $y^* < 0$. For Mode S-II, the magnitude and longitudinal extent of the positive $\tilde{u}^*\tilde{v}^*$ contours are comparable to those of the negative at $y^* > 0$ (figure 7*g*), implying the cancellation of the positive and negative $\tilde{u}^*\tilde{v}^*$ in structural averaging. However, the positive $\tilde{u}^*\tilde{v}^*$ contours at $y^* < 0$ overwhelm the negative in both magnitude and longitudinal extent. The $\langle u_r^* v_r^* \rangle$ contours (figure 8*g*) exhibit similar behaviours. Consequently, $\overline{u^* v^*}$ is very small at $y^* > 0$ and definitely positive at $y^* < 0$ (figure 9*o*); $\overline{\overline{\tilde{u}^*\tilde{v}^*}}$ and $\overline{\overline{\langle u_r^* v_r^* \rangle}}$ are comparable. Because of the occurrence of two streets, the cross-flow distribution of $\overline{u^* v^*}$ for Mode T-I is different from those of the single-street modes. The coherent contribution is comparable to the incoherent above the centreline, but accounts for $\overline{u^* v^*}$ more than the incoherent below the centreline.

The cross-flow distribution of $\overline{u\theta}$ in Mode S-Ia (figure 9*q*) shows two positive peaks with slightly different magnitudes, apparently linked to a small difference in strength between the two rows of vortices (figure 3*a*). The asymmetry about $y^* = 0$ is more evident in $\overline{u\theta}$ for other modes whose vortex strengths on the two sides of the wake differ to a greater extent (figure 3). For Mode S-Ia, the positive $\tilde{u}^*\tilde{\theta}^*$ contours are predominant (figure 7*b*); in contrast, the negative $\langle u_r^* \theta_r^* \rangle$ (figure 8*b*) overwhelms the positive in both spatial extent and magnitude. Furthermore, the maximum magnitude of $\tilde{u}^*\tilde{\theta}^*$ is much larger than that of $\langle u_r^* \theta_r^* \rangle$ (figure 8*b*). Therefore, $\overline{\overline{\tilde{u}^*\tilde{\theta}^*}}$ is pronouncedly positive, whereas $\overline{\overline{\langle u_r^* \theta_r^* \rangle}}$ is negative with a relatively small magnitude, which explains why $\overline{\overline{\tilde{u}^*\tilde{\theta}^*}}$ is larger than $\overline{u\theta}$ at $|y^*| < 3$. Similar explanation applies for the behaviours of $\overline{u\theta}$, $\overline{\overline{\tilde{u}^*\tilde{\theta}^*}}$ and $\overline{\overline{\langle u_r^* \theta_r^* \rangle}}$ at $y^* > 0$ in Modes S-II and T-I. In Mode S-Ib (figure 9*r*) the coherent contribution to $\overline{u\theta}$ is very small since weak vortices could not retain heat.

The cross-stream distribution of $\overline{v\theta}$ is qualitatively antisymmetric about $y^* = 0$ (figure 9*u–x*). The departure from this antisymmetry is small in Modes S-Ia (figure 9*u*), T-I (figure 9*x*) and T-II (figure 12 of Zhou *et al.* 2002), but large in Modes S-Ib (figure 9*v*) and S-II (figure 9*w*). Vortices are effective in transporting heat (e.g. Zhou *et al.* 2002). In fact, $\overline{\overline{\tilde{v}^*\tilde{\theta}^*}}$ accounts for most of $\overline{v\theta}$ for all flow modes except Mode S-Ib, which is characterized by very weak vortices and a smaller $\overline{\overline{\tilde{v}^*\tilde{\theta}^*}}$ than $\overline{\overline{< v_r^* \theta_r^* >}}$ (figure 9*v*). The upper-row vortices are stronger than the lower-row in Modes S-Ib and S-II (figure 3*c*, *e*), leading to the larger magnitude of $\overline{\overline{\tilde{v}^*\tilde{\theta}^*}}$ at $y^* > 0$ than at $y^* < 0$, and subsequently the large departure from antisymmetry in the $\overline{v\theta}$ distribution. Note that the $\overline{\overline{\tilde{v}^*\tilde{\theta}^*}}$ distribution of Mode T-I shows on each side one small peak near $y^* = 0$ and another significantly more pronounced peak near the free stream, which are connected to inner and outer vortices, respectively. Apparently, the low-strength inner vortices could not transport heat as effectively as the outer vortices. A similar observation was made for Mode T-II (cf. figure 12*r* in Zhou *et al.* 2002). It may be inferred that interference between the two vortex streets in Modes T-I and T-II significantly expedites the transport of heat out of vortices as well as the vorticity decay.

	S-I									
Mode	S-Ia		S-Ib		S-II		T-I		T-II	
P^*	1.2		4.0		2.0		4.0		3.0	
α(deg.)	30		10		40		50		90	
x^*	10	20	10	20	10	20	10	20	10	20
$(\overline{\tilde{u}^2}/\overline{u^2})_m$(%)	61	31	19	9	59	31	49	8	36	4
$(\overline{\tilde{v}^2}/\overline{v^2})_m$(%)	71	52	28	27	66	55	69	31	58	23
$(\overline{\tilde{\theta}^2}/\overline{\theta^2})_m$(%)	29	13	15	13	39	30	17	6	15	4
$(\overline{\tilde{u}\tilde{v}}/\overline{uv})_m$(%)	69	54	25	21	50	52	65	21	28	7
$(\overline{\tilde{u}\tilde{\theta}}/\overline{u\theta})_m$(%)	115	88	20	16	94	129	144	27	77	7
$(\overline{\tilde{v}\tilde{\theta}}/\overline{v\theta})_m$(%)	64	53	29	27	60	41	68	21	50	15

TABLE 4. Averaged contributions from the coherent structure to Reynolds stresses, temperature variance and heat fluxes.

5.4. *Streamwise evolution*

The ratio of $\overline{\tilde{q}\tilde{s}}/\overline{qs}$ depends not only on x^*, but also on y^* (figure 9). Thus, an averaged contribution at a fixed x^* from the coherent structure is defined, namely,

$$\left(\frac{\overline{\tilde{q}\tilde{s}}}{\overline{qs}}\right)_m = \int_{-Y^*}^{Y^*} \left|\overline{\tilde{q}\tilde{s}}\right| \mathrm{d}y^* \Big/ \int_{-Y^*}^{Y^*} |\overline{qs}| \mathrm{d}y^*,$$

where $Y^* = 5$ at which $|\overline{qs}|$ is approximately zero. The calculated $(\overline{\tilde{q}\tilde{s}}/\overline{qs})_m$ is summarized in table 4. Generally, $(\overline{\tilde{q}\tilde{s}}/\overline{qs})_m$ is internally consistent with the observations from $\overline{qs}$, $\overline{\tilde{q}\tilde{s}}$ and $\langle\overline{q_r s_r}\rangle$ (figure 9). Firstly, $(\overline{\tilde{v}^2}/\overline{v^2})_m$ is larger than $(\overline{\tilde{u}^2}/\overline{u^2})_m$ or $(\overline{\tilde{\theta}^2}/\overline{\theta^2})_m$, irrespective of flow structures, suggesting a larger coherent contribution to $\overline{v^2}$. Secondly, from $x^* = 10$ to 20, $(\overline{\tilde{\theta}^2}/\overline{\theta^2})_m$ decreases more rapidly, by a factor of about 3, in the twin-street modes than in the single-street modes, indicating again a faster loss of heat owing to interference between the two vortex streets. Thirdly, $(\overline{\tilde{u}\tilde{v}}/\overline{uv})_m$ in Modes S-Ia, S-II and T-I is much larger than that (48 %) in an isolated cylinder wake (Matsumura & Antonia 1993), suggesting more effective momentum transport. Furthermore, although smaller than $(\overline{\tilde{u}\tilde{\theta}}/\overline{u\theta})_m$, $(\overline{\tilde{u}\tilde{v}}/\overline{uv})_m$ is comparable in magnitude to $(\overline{\tilde{v}\tilde{\theta}}/\overline{v\theta})_m$, regardless of the value of x^*, that is, momentum transport is as efficient as heat transport, in distinct contrast with a single-cylinder wake where heat transport is considerably more efficient. Fourthly, $(\overline{\tilde{q}\tilde{s}}/\overline{qs})_m$ of Mode S-Ib is small, compared with other cases, at $x^* = 10$, apparently linked to the weak vortical structures. From $x^* = 10$ to 20, $(\overline{\tilde{q}\tilde{s}}/\overline{qs})_m$ declines more rapidly in Mode S-Ia than in Mode S-II, internally consistent with the vorticity decay (§ 4), because the vortices of both rows in Mode S-Ia are strong and interact with each other more vigorously than in the asymmetric single street of Mode S-II. Mode S-Ib drops in $(\overline{\tilde{q}\tilde{s}}/\overline{qs})_m$ least of all modes, owing to a small variation in vortical structures. In contrast, $(\overline{\tilde{q}\tilde{s}}/\overline{qs})_m$ associated with Modes T-I and T-II declines much more quickly than the single-street modes, reaching a level of about the same as Mode S-Ib at $x^* = 20$, because of the rapid streamwise decay in vortices under vigorous interactions between the streets.

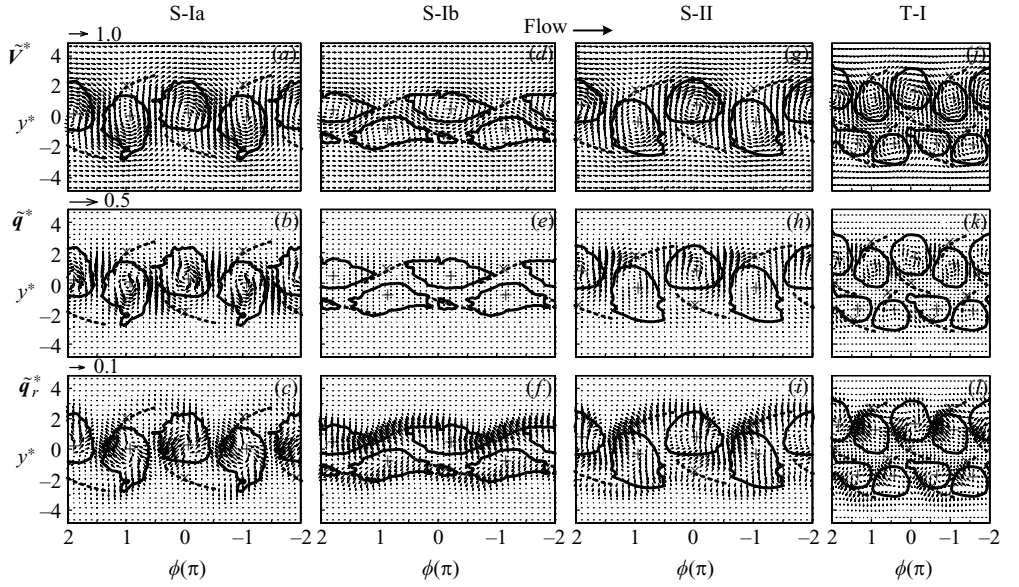

FIGURE 10. Coherent velocity vectors $\tilde{\boldsymbol{V}}^*$ in a reference frame moving at (*a*) $U_c^* = 0.86$, (*d*) 0.81, (*g*) 0.81, (*j*) 0.83, heat flux vectors $\tilde{\boldsymbol{q}}^*$ and incoherent heat flux vectors $\tilde{\boldsymbol{q}}_r^*$ at $x^* = 10$. The broken line indicates the diverging separatrix.

Mode T-II decays faster in $(\overline{\overline{\tilde{q}\tilde{s}}}/\overline{qs})_m$ than Mode T-I, probably because the two streets of the same vortex strength may interact more vigorously with each other.

Srinivas *et al.* (2006) studied numerically a square cylinder wake over $x^* = -5 \sim 15$ and noted that up to $x^* = 11$, the coherent stresses were larger than their incoherent counterparts. The same observation is made here, which is reasonable since the near wake is, in general, characterized by strongly coherent vortices. However, the incoherent stresses may exceed in magnitude the coherent for Mode S-Ib. This is not unexpected in view of very weak vortices in this mode (figure 3). It should be mentioned that at $x^* = 20$, the incoherent contributions (not shown in table 4), e.g. $(\overline{\langle u_r^2 \rangle}/\overline{u^2})_m$, $(\overline{\langle v_r^2 \rangle}/\overline{v^2})_m$ and $(\overline{\langle u_r v_r \rangle}/\overline{uv})_m$, account for more towards the Reynolds stresses than do the coherent. The only exception is $\tilde{v}^2$, which exceeds slightly its incoherent counterpart in Modes S-Ia and S-II at $x^* = 20$, probably owing to the present phase-averaging technique, which identifies vortices based on the v-signal, thus overestimating the coherent contribution in the lateral direction.

6. Further discussion

Heat transport characteristics of the four flow modes may be further explored by examining the coherent heat flux vector $\tilde{\boldsymbol{q}}^* = (\tilde{u}^*\tilde{\theta}^*, \tilde{v}^*\tilde{\theta}^*)$ (figure 10*b*, *e*, *h*, *k*) and incoherent heat flux vector $\tilde{\boldsymbol{q}}_r^* = (\langle u_r^*\theta_r^* \rangle, \langle v_r^*\theta_r^* \rangle)$ (figure 10*c*, *f*, *i*, *l*), along with the velocity vector $\tilde{\boldsymbol{V}}^* = (\overline{U}^* + \tilde{u}^* - U_c^*, \tilde{v}^*)$ (figure 10*a*, *d*, *g*, *j*). Velocity vectors are viewed in a reference frame translating at U_c. One reference vector of a specified length is given at the left-hand upper corner of the $\tilde{\boldsymbol{q}}^*$, $\tilde{\boldsymbol{q}}_r^*$ or $\tilde{\boldsymbol{V}}^*$ plots in figure 10 to indicate the correspondence between the length and magnitude of a vector.

The relatively long vectors of $\tilde{\boldsymbol{q}}^*$ are mostly aligned with $\tilde{\boldsymbol{V}}^*$ within each vortex except Mode S-Ib whose vortex strength is very low. On the other hand, the

low-strength vortices are associated with relatively short $\tilde{\boldsymbol{q}}^*$, including Mode S-Ib (figure 10*e*) and vortices below the centreline of Modes S-II (figure 10*h*) and T-I (figure 10*k*), that is, the strong coherent motion retains heat and the weak loses heat rapidly. The relatively long vectors of $\tilde{\boldsymbol{q}}^*$ also occur in the alleyway between two oppositely signed vortices, with the upstream one characterized by strong coherent motion, and point towards the free stream, oppositely to $\tilde{\boldsymbol{V}}^*$. These vectors indicate that cold fluid is approximately evenly entrained from both sides into the wake in Modes S-Ia (figure 10*b*) and T-II (refer to figure 14*h* in Zhou *et al.* 2002), but predominantly from the downstream cylinder side in Modes S-II (figure 10*h*) and T-I (figure 10*k*). The entrainment of cold fluid into the wake is barely discernible in Mode S-Ib (figure 10*e*) because of very weak coherent motion.

The incoherent heat flux vectors, $\tilde{\boldsymbol{q}}_r^*$, behave differently from $\tilde{\boldsymbol{q}}^*$. They do not seem to show any correlation with $\tilde{\boldsymbol{q}}^*$ within the vortex, and are approximately normal to the diverging separatrix in the saddle region since the temperature front along the diverging separatrix is largest (Matsumura & Antonia 1993). The vectors in Mode S-Ia show similar behaviours to their counterparts in an isolated cylinder wake (cf. figure 8*g* in Matsumura & Antonia 1993 and figure 14*c* in Zhou *et al.* 2002). Downstream within the vortex at $\phi = 0$, $\tilde{\boldsymbol{q}}_r^*$ largely points upward toward the free stream (figure 10*c*), suggesting the association of either $v_r < 0$ with $\theta_r < 0$ or $v_r > 0$ with $\theta_r > 0$. The latter is more likely, corresponding to the loss of heat owing to the incoherent motion. Upstream within the vortex, relatively long vectors point downwards ($\langle v_r^* \theta_r^* \rangle < 0$) and upstream ($\langle u_r^* \theta_r^* \rangle < 0$), that is, $u_r < 0$ tends to correspond to $\theta_r > 0$, and $v_r > 0$ (or $v_r < 0$) is associated with $\theta_r < 0$ (or $\theta_r > 0$); these vortices appear crossing the vortex border. The negative $\langle v_r^* \theta_r^* \rangle$ is most probably due to the assimilation of cold potential fluid ($\theta_r < 0$) drawn into this vortex from the free stream by the vortex at $\phi = 1$ on the other side of the wake. Similar observations are also made for the vortices at $\phi = \pm 1$, though relatively long vectors upstream within the vortices cross the vortex border considerably more evidently than the upper-row vortex. It may be concluded that the incoherent motion plays a key role in transporting heat out of vortices and drawing cold fluid into vortices.

For Mode S-Ib, the incoherent heat flux vectors (figure 10*f*) behave distinctly from Mode S-Ia, pointing largely towards the free stream, in particular, those normal to and intersecting with the diverging separatrix, suggesting the association of $\theta_r > 0$ with $v_r > 0$ for $y^* > 0$ and with $v_r < 0$ for $y^* < 0$ or the association of $\theta_r < 0$ with $v_r < 0$ for $y^* > 0$ and with $v_r > 0$ for $y^* < 0$. The former results from heat transport out of vortices or turbulent heat diffusion, while the latter from the entrainment of cold fluid into the wake because of incoherent motion.

The vectors, $\tilde{\boldsymbol{q}}_r^*$, in Mode S-II show more asymmetry about the centreline because of the significant departure of the two rows of vortices from anti-symmetry (figure 3*e*). Those corresponding to the lower-row vortices resemble their counterparts of Mode S-Ia. This is, however, not the case for the upper-row vortices. First, relatively long vectors downstream within the vortex, which point upward towards the free stream, cross the vortex border, which is not so evident in Mode S-Ia. Secondly, in contrast to Mode S-Ia, the vectors are short upstream within the vortex, but exhibit more similarity in the saddle region to those in Mode S-Ib. The vectors, near the saddle, normal to and intersecting with the diverging separatrix are rather long, suggesting considerable heat transport in the saddle region, which is internally consistent with the peak at $y^* \approx 2$ in $\overline{v_r^* \theta_r^*}$ (figure 9*w*).

Vectors, $\tilde{\boldsymbol{q}}_r^*$, in each street of Mode T-I (figure 10*l*) behave similarly to those of Mode S-Ia, though there is a difference due to interference between the streets. In general, relatively long vectors occur upstream of the vortices, regardless of the inner or the outer, which point upstream towards the free stream for the inner vortices, but towards the centreline for the outer. The former cross the vortex border much more evidently than the latter, probably because the central region about $y^* = 0$ is of higher temperature (figure 2*h*), indicating that the inner vortices lose heat more rapidly than the outer, corroborating the earlier observations based on figure 9(*x*).

Based on $\tilde{\boldsymbol{V}}^*$, $\tilde{\boldsymbol{q}}^*$ and $\tilde{\boldsymbol{q}}_r^*$, the flow structure and heat transport characteristics at $x^* = 10$ are summarized in figure 11. The flow structure is sketched, based on flow-visualization data in Part 1, on the left-hand side of each plot, where typical initial relationships between shear layers around the cylinders are also included for each flow mode. Apparently, the relationships are distinct from one mode to another. The effect of initial conditions may persist even in the self-preserving turbulent shear flows, including wakes (e.g. Wygnanski *et al.* 1986; George 1989; Zhou & Antonia 1995). Naturally, the flow structure and heat transport behind two staggered cylinders may differ from one mode to another in view of their distinct initial conditions.

Both flow structure and heat transport of Mode S-Ia (figure 11*a*) are very similar to the isolated cylinder case (Matsumura & Antonia 1993). Cold fluid is drawn equally into the wake from either side of the vortex street, namely, from free stream 1 under the combined coherent motions of vortices A and C through the alleyway downstream of vortex A and from free stream 2 owing to the joint coherent motions of vortices B and A via the alleyway downstream of vortex B. As a result, the coherent heat flux is significant in the alleyways. Heat loss is mostly due to the incoherent motion, including heat transport out of quadrant I of vortex A and quadrant IV of vortex B and the assimilation of cold fluid into quadrant III of vortex A and quadrant II of vortex B by vortices on the other side of the wake.

Because of weak vortices, the incoherent heat transport in Mode S-Ib (figure 11*b*) overwhelms the coherent; the entrainment of cold fluid into the wake is insignificant, leading to a barely discernible coherent heat flux in the alleyway between oppositely signed vortices, compared with Mode S-Ia. Furthermore, the lateral incoherent heat flux contributes mostly to the net heat transport out of vortices, which occurs largely in the two quadrants of vortices near the free stream.

Heat transport for Mode S-II (figure 11*c*) is distinct from that for Mode S-Ia or S-Ib. The coherent motion originating from the downstream cylinder is significantly stronger than from the upstream cylinder. Accordingly, vortex A plays a major role in drawing cold fluid from free stream 1 into the wake, resulting in a considerable coherent heat flux in the alleyway downstream of vortex A. In contrast, cold fluid entrained from free stream 2 by vortex B is less and subsequently the coherent heat flux in the alleyway between B and A is significantly weaker. Similarly to Mode S-Ia, the incoherent motion leads to considerable heat transport out of quadrant I of vortex A and quadrant IV of vortex B, and the assimilation of cold fluid, entrained by vortex A, into quadrant II of vortex B. Because vortex B is weak, the assimilation of cold fluid into quadrant III of vortex A is not so evident.

Each street of Mode T-I (figure 11*d*) behaves qualitatively similarly to Mode S-Ia in the flow structure and heat transport. However, interference between the two streets of different vortex strengths does cause a difference. Being characterized by stronger vortices, the upper street entrains more cold fluid, mainly via its outer vortices (vortex A), from free stream 1 than the lower from free stream 2, resulting in a larger

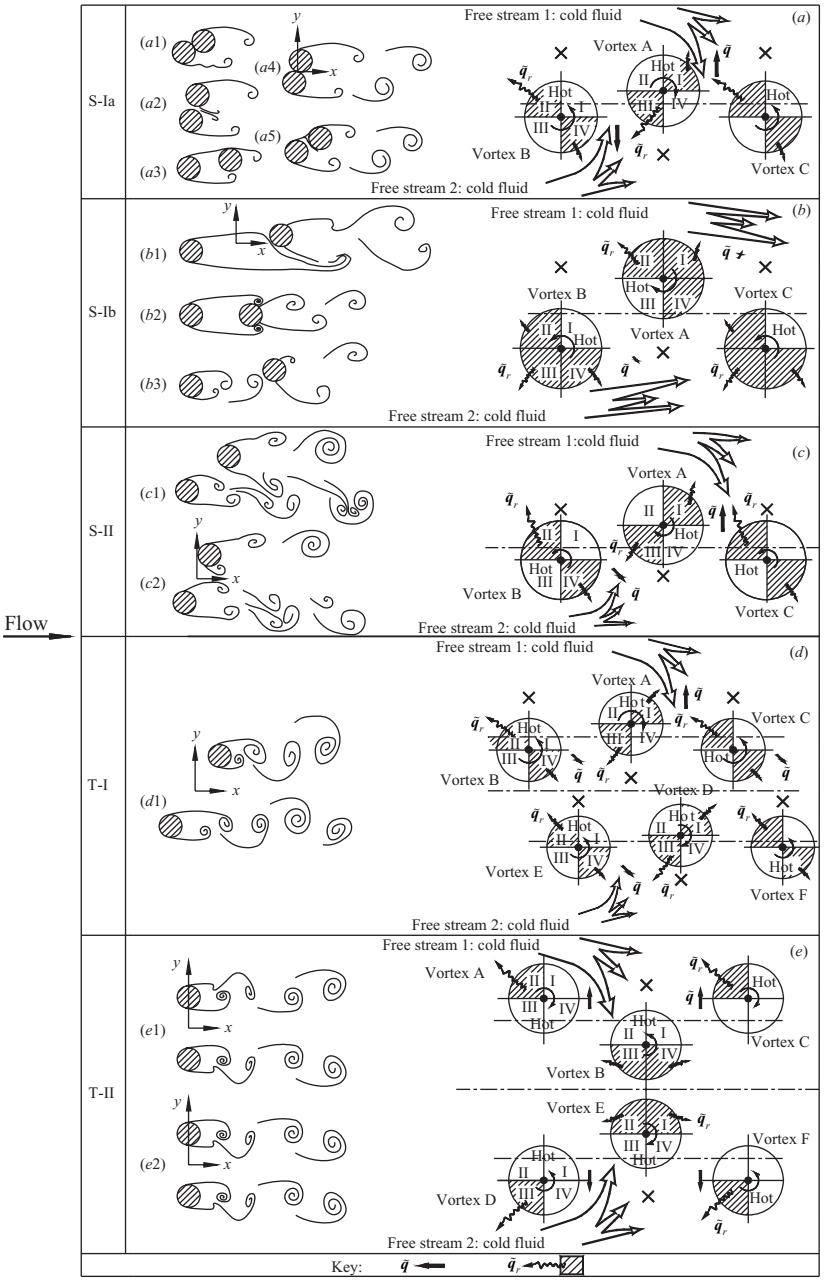

FIGURE 11. Summary sketch of the flow structures and heat transport at $x^* = 10$. (*a*) Mode S-Ia; (*b*) S-Ib; (*c*) S-II; (*d*) T-I; (*e*) T-II.

coherent heat flux in the alleyway between vortices A and C than that between E and D. Furthermore, heat loss from quadrant II of the inner vortex B (or C) owing to incoherent motion exceeds appreciably that from quadrant III of the outer vortex A, contributing to the rapid loss of heat from the inner vortices. The same is observed in the lower street. Heat transport for Mode T-II (figure 11*e*) has been discussed in detail in Zhou *et al.* (2002, figure 15*b*), and thus is not repeated here.

7. Conclusions

Four typical flow structures, i.e. Modes S-I, S-II, T-I and T-II, are identified in the wake of two staggered circular cylinders, each exhibiting distinct heat and momentum transport from others.

Mode S-I is characterized by a single vortex street of reasonable antisymmetry about the centreline, and is further divided into S-Ia and S-Ib. The maximum vorticity concentration of S-Ia exceeds 80 % of that in an isolated cylinder wake. Mode S-Ib is characterized by very weak vortices, with the maximum vorticity concentration not exceeding 40 % of that in an isolated cylinder wake; the vortices are longitudinally stretched and their formation is probably not completed at $x^* = 10$. Mode S-II is a single street asymmetric about the wake centreline, with the vortex strength in one row (associated with the downstream cylinder) double that in the other (associated with the upstream cylinder). Mode T-I is characterized by two distinct streets of different vortex frequencies, which persist even beyond $x^* = 10$. The vortex strength in the downstream-cylinder-generated street is about 40% higher than that in the upstream-cylinder-generated street. Mode T-II consists of two coupled streets of the same vortex strength and frequency ($St \approx 0.21$; e.g. Zhou *et al.* 2002).

The four typical flow structures are distinct in the streamwise evolution. The phase-averaged maximum vorticity concentration of Mode S-Ia drops by about 40 % from $x^* = 10$ to 20 owing to interactions between the cross-stream opposite-signed vortices. This drop is smaller than that (58 %) in an isolated cylinder wake (Zhou *et al.* 2002), which is ascribed to the longer vortex wavelength of Mode S-Ia. In Mode S-Ib, the longitudinally stretched opposite-signed vortices, though weak, are liable to interact with each other, resulting in a 40 % drop in $\tilde{\omega}^*_{max}$. The two rows of vortices in Mode S-II display different decay rates, their maximum vorticity concentration dropping by 43 % and 29 %, respectively. Owing to vigorous interactions between the two streets, Modes T-I and T-II decay in the vortex strength more rapidly than the single-street modes; the outer vortices experience a drop in $\tilde{\omega}^*_{max}$ by about 60 % from $x^* = 10$ to 20, with the inner by 80 % for Mode T-II and even vanished for Mode T-I. The vorticity flux density vectors indicate that inner vortices interact not only with the outer vortices generated by the same cylinder, but also with vortices generated by the other.

Turbulent entrainment differs from one flow mode to another. While brought in equally from either side of the wake in antisymmetric Mode S-Ia or symmetric T-II, the free-stream fluid is largely entrained into the wake by downstream-cylinder-generated vortices (which are stronger than upstream-cylinder-generated ones) in asymmetric Modes S-II and T-I. Owing to weak vortices, the entrainment motion is very weak in Mode S-Ib.

The distinct flow structures naturally lead to a difference in the behaviours of Reynolds stresses and heat fluxes. It is worth pointing out that, although the two cylinders in Mode S-Ia behave like a single body, generating a vortex street that appears to resemble an isolated cylinder wake, the momentum transports between the flows are distinct. The difference between the flow modes is further reflected in the coherent contribution from vortices to Reynolds stresses and heat fluxes. In general, vortices transport heat more efficiently than momentum in a two-staggered-cylinder wake, as observed in an isolated cylinder wake (Matsumura & Antonia 1993). However, momentum transport can be significant in Modes S-Ia, S-II and T-I, for exceeding an isolated-cylinder case. The averaged coherent contribution in Mode S-Ia at $x^* = 10$ is largest of all the modes, amounting to about 61 % to $\overline{u^2}$, 71 % to $\overline{v^2}$, 29 % to $\overline{\theta^2}$, 69 % to $\overline{uv}$ and 64 % to $\overline{v\theta}$. In contrast, they are lowest in Mode S-Ib, only 19 %, 28 %, 15 %, 25 % and 29 %, respectively. These contributions are

59 %, 66 %, 39 %, 50 % and 60 %, respectively, in Mode S-II and 49 %, 69 %, 17 %, 65 % and 68 %, respectively, in Mode T-I. From $x^* = 10$ to 20, $(\overline{\overline{\tilde{q}\tilde{s}}}/\overline{qs})_m$ decays faster in the symmetric/antisymmetric modes than in the asymmetric, that is, Modes S-Ia and T-II decay faster than S-II and T-I, respectively. Mode S-Ib decays slowest in $(\overline{\overline{\tilde{q}\tilde{s}}}/\overline{qs})_m$. The heat transport of twin-street modes is accelerated owing to interactions between the streets, resulting in a rapid drop, a factor of about 3, in the coherent contribution to $\overline{v\theta}$ from $x^* = 10$ to 20, along with the rapid decay in the vortex strength. Furthermore, the inner vortices of Modes T-I and T-II lose heat faster than the outer, leading to a negligible contribution to $\overline{v\theta}$ at $x^* = 10$.

Y. Z. wishes to acknowledge support given to him by the Research Grants Council of the Government of the HKSAR through Grants PolyU 5280/04E. Dr. H. F. Wang's contribution to experiments is acknowledged.

REFERENCES

Akbari, M. H. & Price, S. J. 2005 *J. Fluids Struct.* **20**, 533–554.
Alam, M. M. & Sakamoto, H. 2005 *J. Fluids Struct.* **20**, 425–449.
Bisset, D. K., Antonia, R. A. & Browne, L. W. B. 1990 *J. Fluid Mech.* **218**, 439–461.
Cantwell, B. & Coles, D. 1983 *J. Fluid Mech.* **136**, 321–374.
George, W. K. 1989 In *Recent Advances in Turbulence* (ed. R. E. Arndt & W. K. George), 39–73. Hemisphere.
Gu, Z. & Sun, T. 1999 *J. Wind Engng Indust. Aerodyn.* **80**, 287–309.
Hori, E. 1959 *Proc. 9th Japan National Congress for Applied Mechanics*, III-11, 231–234.
Hu, J. C & Zhou, Y. 2008 Flow structure behind two staggered circular cylinders. Part 1. Downstream evolution and classification. *J. Fluid Mech.* **607**, 51–80.
Huang, J. F., Zhou, Y. & Zhou T. M. 2006 *Exps. Fluids*, **40**, 884–896.
Hussain, A. K. M. F. & Hayakawa, M. 1987 *J. Fluid Mech.* **180**, 193–229.
Ishigai, S., Nishikawa, E., Nishimura, E. & Cho, K. 1972 *Bull. JSME* **15**, 949–956.
Ishigai, S., Nishikawa, E. & Yagi, E. 1973 In *Proc. Symp. on Marine Engineering, Tokyo, Japan*, pp. 1-5-2–1-5-33.
Kiya, M. & Matsumura, M. 1985 *Bull. JSME* **28**, 2617–2624.
Kiya, M., Arie, M., Tamura, H. & Mori, H. 1980 *Trans. ASME I: J. Fluids Engng* **102**, 166–173.
Kolář, V., Lyn, D. A. & Rodi, W. 1997 *J. Fluid Mech.* **346**, 201–237.
Mahir, N. & Rockwell, D. 1996 *J. Fluids Struct.* **10**, 473–489.
Matsumura, M. & Antonia, R. A. 1993 *J. Fluid Mech.* **250**, 651–668.
Mumford, J. C. 1982 *J. Fluid Mech.* **118**, 241–268.
Mumford, J. C. 1983 *J. Fluid Mech.* **137**, 447–456.
Price, S. J. & Païdoussis, M. P. 1984 *J. Wind Engng Indust. Aerodyn.* **17**, 329–347.
Rinoshika, A. & Zhou, Y. 2005 *J. Fluid Mech.* **524**, 229–248.
Roshko, A. 1954 *NACA TN* 3169.
Shraiman, B. I. & Siggia, E. D. 2000 *Nature* **405**, 639–646.
Srinivas, Y., Biswas, G., Parihar, A. S. & Ranjan, R. 2006 *J. Engng Mech.* **132**, 793–793.
Sumner, D., Price, S. J. & Païdoussis, M. P. 2000 *J. Fluid Mech.* **411**, 263–303.
Sumner, D., Richards, M. D. & Akosile, O. O. 2005 *J. Fluids Struct.* **20**, 255–276.
Suzuki, N., Sato, H., Iuchi, M. & Yamamoto, S. 1971 In *Wind Effects on Buildings and Structures, Intl Wind Conf., Tokyo*, Part II, pp. 20-1–20-10.
Wang, Z. J. & Zhou, Y. 2005 *Intl J. Heat Fluid Flow.* **26**, 362–377.
Warhaft, Z. 2000 *Annu. Rev. Fluid Mech.* **32**, 203–240.
Wygnanski, I., Champagne F. & Marasli, B. 1986 *J. Fluid Mech.* **168**, 31–71.
Wygnanski, I. & Petersen, R. A. 1987 *AIAA J.* **25**, 201–213.
Zdravkovich, M. M. 1977 *Trans. ASME I: J. Fluids Engng* **199**, 618–633.
Zdravkovich, M. M. 1985 *J. Sound Vib.* **101**, 511–521.

Zdravkovich, M. M. 1987 *J. Fluids Struct*. **1**, 239–261.
Zhou, Y. & Antonia, R. A. 1994 *J. Fluid Mech.* **275**, 59–81.
Zhou, Y. & Antonia, R. A. 1995 *Exps. Fluids* **19**, 112–120.
Zhou, Y. & Yiu, M. W. 2006 *J. Fluid Mech.* **548**, 17–48.
Zhou, Y., Antonia, R. A. & Tsang, W. K. 1998 *Exps. Fluids* **25**, 118–125.
Zhou, Y., Wang, Z. J., So, R. M. C., Xu, S. J. & Jin, W. 2001 *J. Fluid Mech.* **443**, 197–229.
Zhou, Y., Zhang, H. J. & Yiu, M. W. 2002 *J. Fluid Mech.* **458**, 303–332.